On an Electron Spin Resonance Spectrometer for Quantum Information Processing

by

Jeremy Chamilliard

A thesis
presented to the University of Waterloo
in fulfillment of the
thesis requirement for the degree of
Master of Science
in
Physics

Waterloo, Ontario, Canada, 2011

I hereby declare that I am the sole author of this thesis. This is a true copy of the thesis, including any required final revisions, as accepted by my examiners.

I understand that my thesis may be made electronically available to the public.

Abstract

Electron spins are an attractive candidate for an implementation of quantum information processing (QIP) due to high polarization, fast control and long coherence times. Control in electron spin resonance benefits from extensive experience in liquid-state nuclear magnetic resonance QIP, and microwave and RF technology from industry. This thesis details the design and construction of an electron spin resonance spectrometer specifically for research in quantum information processing, including the microwave electronics and variable temperature resonators and probes. We also begin to evaluate our spectrometer using a novel technique known as randomized benchmarking which extracts a figure of merit relevant to QIP.

Acknowledgements

I would like to acknowledge my supervisor, Prof. Raymond Laflamme for taking a chance with me, and for allowing me to be a part of the Institute for Quantum Computing and his research group. I also thank Prof. Jonathan Baugh and Prof. Bill Power for their roles on my advisory committee, and Prof. Adrian Lupascu for being a part of my defence comittee.

I would like to acknowledge Michael Ditty for recruiting me to my initial undergraduate research project which eventually became this degree and thesis. I am also indebted to Wendy Reibel, without whose assistance I would not have made it this far.

For help with the project, I thank Mike Ditty, Jonathan Baugh, Mike Zhang and Colm Ryan. Colm's breadth of knowledge was invaluable, and his assistance and motivation is directly responsible for the progress of the project. I also thank Jonathan Hodges, Jamie Yang, Mohamed Abutaleb and David Cory for sharing their ESR designs and experience with us.

I acknowledge Prof. Art van der Est from Brock University for the use of his commercial ESR spectrometer, Dr. John Morton and Stephanie Simmons from the University of Oxford for their collaboration on the randomized benchmarking project, and Dr. Kyriakos Porfyrakis from Oxford for synthesis and purification of the $N@C_{60}$ sample.

I thank the Canadian Foundation for Innovation for financial assistance of our ESR research at IQC.

Table of Contents

List of Tables

List of Figures

Chapter 1

Quantum Information Processing with Electron Spins

Electron spin resonance (ESR), a spectroscopic technique now 65 years old, is today an emerging area of quantum information processing. Certain paramagnetic materials, such as atomic impurities in a solid lattice are promising implementations for quantum information processing (QIP) due to extremely long coherence times at room temperature. Electron spin QIP implementations benefit from extensive control experience developed in liquid-state NMR QIP and fabrication experience from the eld of semiconductors.

Common impurity spin ESR qubits include

- Colour centres in diamond, e.g. nitrogen-vacancy centres.

- Dopant atoms in semiconductors, e.g. phosphorus in silicon.

- Ions incarcerated by fullerene cages (endohedral fullerenes), e.g. nitrogen incarcerated fullerene

- Unpaired electrons at radiation induced defects, e.g. gamma irradiated malonic acid

- Rare earth ions in dielectric crystals

- Free radicals in molecular crystals

1.1 Electron Spin Resonance

Electron spin resonance arises from the interaction between the electron magnetic dipole moment and an applied magnetic field. The magnetic energy of the interaction is the dot product of the electron moment, $\vec{\mu_e}$ and the applied field $\vec{B_0}$,

$$\hat{\mathcal{H}} = -\vec{\mu_e} \cdot \vec{B_0}$$
$$\hat{\mathcal{H}} = \frac{g_e \mu_B}{\hbar} B_0 \hat{S}_z \tag{1.1}$$

In NMR convention,

$$\hat{\mathcal{H}} = -\gamma_e B_0 \hat{S}_z \tag{1.2}$$

where g_e is the electron g-factor and μ_B is the Bohr magneton. $g_e \mu_B B_0 / \hbar$ is the Larmor frequency of the spin in this field. The Larmor frequency is probed by ESR spectroscopy. The resonant condition can be tuned in either parameter to meet any fixed value of the other, i.e.:

$$f = \left(\frac{g_e \mu_B}{h}\right) B_0 \approx 2.8 \frac{\text{GHz}}{\text{kG}} \text{ , or} \tag{1.3}$$
$$B_0 = \left(\frac{h}{g_e \mu_B}\right) f \approx 0.357 \frac{\text{kG}}{\text{GHz}} \tag{1.4}$$

ESR spectroscopy is typically performed in one of the standard microwave frequency bands[1] listed in Table 1.1. By far the most commonly used frequency is X-band, roughly 10GHz, corresponding to magnetic field strengths around 0.35 Tesla (T) or 3500 Gauss (G). X-band has traditionally provided a good compromise between sensitivity, convenience and cost of microwave components [57]; however with improvements in microwave technology, the historical abundance of resonators for this band may be the reason it remains dominant in EPR spectroscopy [24].

2
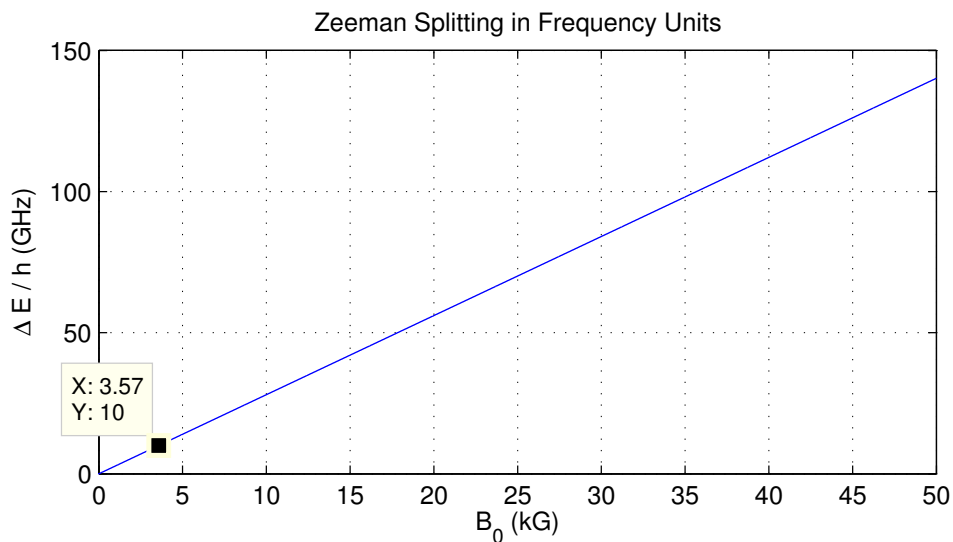
Figure 1.1: Electron Zeeman splitting. The vertical axis represents $\Delta E/h$, in units of frequency. The commonly used 10GHz / 3.57kG, X-band point is highlighted.

Band Designation	Frequency Range (GHz)	ESR Field (kG)
L	1–2	0.5
S	2–4	1
C	4–8	2
X	8–12	3.5
Ku	12–18	5
K	18–26.5	8
Ka	26.5–40	12
Q	30–50	14
U	40–60	18
V	50–75	22
E	60–90	26
W	75–110	33
mm	110–300	100

Table 1.1: Standard ESR spectrometer frequencies and magnetic field strengths. 10kG is equal to 1T.

1.2 QIP with ESR

In 2000, David DiVincenzo published a set of five criteria for any physical realization of quantum information processing[12], now well-accepted by researchers. The DiVincenzo criteria are:

1. A scalable physical system with well characterized qubits

2. The ability to initialize the state of the qubits to a simple fiducial state

3. Long relevant decoherence times, much longer than the gate operation time

4. A "universal" set of quantum gates

5. A qubit-specific measurement capability

1.2.1 State-of-the-Art

Signicant progress has been made in the eld of ESR impurity spin QIP over the past decade. Single impurity spin qubits can now be isolated, initialized, controlled and measured.

1. A scalable physical system with well-characterized qubits

   - Several demonstrations of N-V centre qubit control and coupling to nearby nitrogen [16] and ^{13}C [59, 26, 44, 13, 42, 29, 48] qubits have been achieved. Recent progress in ultra-pure, spin-depleted diamond fabrication has reduced decoherence effects to such an extent that spins may be separated by up to 100nm and still be coherently coupled [19, 5]. Separations of this order could eventually allow individual optical addressing and thus a scalable array of qubits.

   - The phosporus in silicon qubit may be the Zeeman splitting of electron and/or nuclear spins associated with a phophorus dopant atom in a silicon lattice. Scaling beyond the two qubits associated with the impurity will require nearby dipolar or electron-mediated coupled spins. Couplings could potentially be mediated by additional electric gates as in the proposal by Kane [32]. Charge qubits based on donor impurities have also been proposed, utilizing surface electrodes and radio-frequency single-electron transistors. [23]

- The nitrogen endohedral fullerene ($N@C_{60}$) provides an electronic spin-3/2 qubit and a possible nuclear spin qubit created by a nitrogen atom implanted in a fullerene cage. Some proposals for scalability being investigated include arrangement on substrates, synthesis of endohedral fullerene dimers, and carbon nanotube 'peapod' arrays of endohedral fullerenes. [54, 20, 53, 21]

2. The ability to initialize the state of the qubits to a simple fiducial state

- Initialization of the N-V centre qubit can be accomplished by utilizing a spin-selective transition to a metastable state between optical excited and ground states. In addition, the spin state of individual spins can be measured optically. Initialization has also been extended to an associated ^{15}N nuclear spin and coupled ^{13}C spins [18].

- Owing to the large magnetic moments of electrons, qubits in Si:P and $N@C_{60}$ can be initialized to their ground state at experimentally accessible magnetic fields and temperatures. Strongly polarized electron spins can then be used to polarize nuclear spins through a SWAP operation [40].

3. Long (relative) decoherence times, much longer than the gate-operation time

- Current microwave control in electron spin systems typically allows for gates on the order of 100ns. By contrast, decoherence times have been measured on the order of milliseconds for most impurity spins—a difference of roughly 10,000 times. Advances in spin-depleted host materials are mostly responsible for the incredible coherence times now provided by impurity spins—isotopically enriched and purified ^{12}C diamonds for N-V centres, and ^{28}Si for Si:P.

4. A universal set of quantum gates

- Like NMR, impurity spin qubits may be controlled by electromagnetic pulses, normally RF for nuclear and microwave frequency for electron spins. For a single qubit, universal control is equivalent to arbitrary rotations on the Bloch sphere, which can be realized by varying the power, duration, and the phase of the microwave radiation applied to the system.

- Multiple-qubit interactions can be provided by spin couplings, which may be always-on or mediated by electrodes in some proposals.
- High fidelity qubit control has been demonstrated in N-V centres [50, 48, 17, 26, 33], Si:P [40] and N@C$_{60}$ [37].

5. A qubit-specific measurement capability

- In N-V centres, the spin state of a single electron qubit has been measured at room temperature using optical spectroscopy. Due to the energy level structure, an N-V centre will only fluoresce after exciting a spin-0 sublevel of the triplet, which can be detected by confocal microscope. [27, 28]
- Single Si:P qubit readout has been proposed via single-electron transistor charge detection, and proof of principal demonstrations have been conducted.[23, 2, 49]

1.3 Coherent Control

In the Bloch sphere picture shown in 1.2, a pulsed-ESR experiment entails rotations of the electron spin magnetization vector about the sphere. This is achieved experimentally by applying resonant microwave pulses of precise amplitude, phase and duration. The pulse generates an oscillating magnetic field, B$_1$, in the resonator that is perpendicular to the applied magnetic field B_0. For pulses resonant with the Larmor frequency, the RF Hamiltonian can be expressed[56] as

$$\hat{\mathcal{H}}_{RF} = \omega_1 \cos(\phi_p)\frac{\sigma_x}{2} + \omega_1 \sin(\phi_p)\frac{\sigma_y}{2} \tag{1.5}$$

With the nutation frequency, $\omega_1 = g\mu_B B_1/\hbar$. Thus the effective *axis* of rotation ϕ is set by the phase of the microwave radiation, and for a pulse of constant amplitude, the *angle* of rotation is related to the amplitude and duration of the pulse by:

$$\theta_{nut} = \frac{g\mu_B B_1}{\hbar}\tau \tag{1.6}$$

Where B_1 is the amplitude of the magnetic field generated by the microwave pulse and τ is the duration. For high fidelity coherent control, it is important that the time to
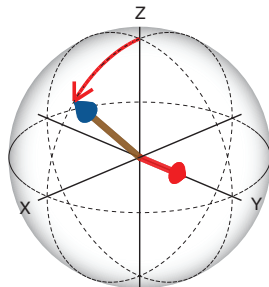
Figure 1.2: A simple coherent rotation visualized on the Bloch sphere. Here a simple pulse along the +Y axis causes the magnetization vector to rotate towards the +X axis.

(a)   (b)
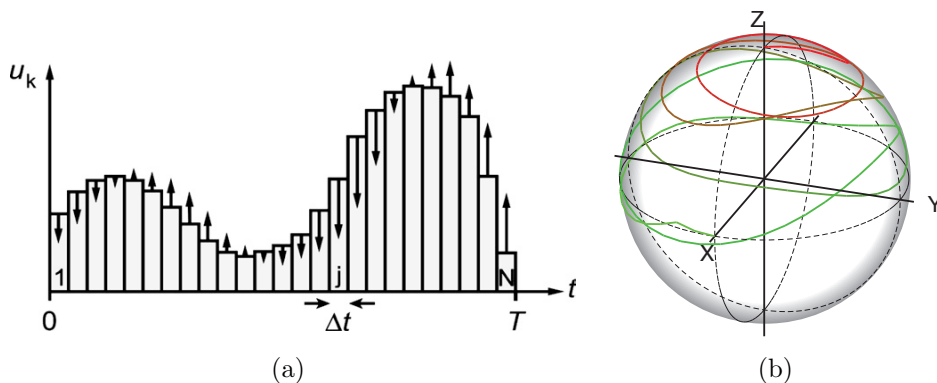
Figure 1.3: (a) An initial guess to a discretized pulse shape as part of the GRadient Ascent Pulse Engineering (GRAPE) algorithm for optimal control [34]. (b) The complex trajectory of the magnetization vector under the action of a GRAPE pulse, which was solved to be optimal for a desired transformation in a particular spin system. The result is a simple rotation of the vector from $+Z$ to $+X$ (red to green).

implement these pulses be much shorter than decoherence in the system. Typical timescales of decoherence in electron spin systems are tens to hundreds of microseconds, thus we desire the nutation rates to be the order of tens of MHz.

With sufficiently advanced spectrometer technology, techniques such as optimal control of coupled spin dynamics [34], can be used to find pulses that effect complex unitary gates on a system of coupled spins. Figure 1.3(a) shows a discretized initial pulse shape guess as part of the GRadient Ascent Pulse Engineering (GRAPE) algorithm. (b) shows an example of a complex trajectory the spin may trace out under an optimal control pulse.

7

Chapter 2

A Pulsed ESR Spectrometer for QIP

A pulsed ESR spectrometer will allows the pursuit of high-fidelity coherent control in the electron spin qubit system. We have designed and built a pulsed spectrometer around the stringent requirements of quantum information processing. For high fidelity operations, our spectrometer must offer the utmost stability, precision, flexibility and sensitivity. These challenges are addressed in this chapter.

2.1 Magnetic Field Control

The static applied magnetic field for ESR experiments is generated by a pre-existing Varian electromagnet system. The V3900 electromagnet has a 6 inch air gap and very large, 12 inch diameter, cylindrical pole faces which provide good field uniformity. The magnet has a hot resistance of 0.18Ω, and requires approximately 110 Amps to generate a field of 3.4kG at the centre of the air gap. A Varian VFR2703 20kW power supply provides the DC magnet current, and can achieve fields of up to about 0.5T / 5kG. At these fields, only a fraction of the maximum power is used ($\sim$2kW), however the current output of the supply is limited to 142A and appears to be a poor match to the electromagnet. A Varian Fieldial Mark I controller regulates the power supply output to set and maintain the desired magnetic field. Manual dials allow for setting the field directly in kG, and configuring field sweeps of varying size and duration. The Fieldial controller uses a Hall probe to regulate the field strength and should provide isolation from changes in line voltages, load impedance, noise

and temperature drifts. The original specification is for stability of better than 1ppm. Both the electromagnet and power supply are water cooled using a Lytron Kodiak RC030 air-cooled recirculating chiller which has a 3450W capacity at 20°C and maintains the water temperature to ±0.1°C.

Unfortunately, the magnet regulation system as configured does not give satisfactory field stability, an example of which is shown in Figure 2.1. The system has been observed to suffer both short fluctuations and longer drifts. A possible cause of the long term drift is a failure of the controller to compensate for heating of the Hall probe as the magnet and surrounding air temperature warm. The recirculating chiller which should remove heat from the magnet and power supply is exhausting waste heat into the air surrounding the experiment in the current facilities, which do not have thermostat controls in individual rooms to compensate. The age of the magnet system (*ca.* 1968), lack of documentation of the instrument and historical modifications and the complexity of the electronics has made it difficult to ensure the system is calibrated properly. In addition to the stability concerns, we desire computerized and digital control of the field and sweep settings in a modern spectrometer, enabling better precision and automation.

To remedy these issues, a Danfysik MPS 854 power supply and controller has been purchased. The new power supply capacity is 6.4kW with a maximum current of 160A, and has an upgraded stability option giving better than 0.1ppm over 30minutes and 2ppm over 8 hours. To our knowledge this is the highest stability available in an electromagnet power supply. A standard RS-232 interface for computer programming of the current and sweep parameters is provided. The MPS 854 is current-regulated instead of field-regulated which reduces noise in the system from the field transducer. Based on the convenience and performance of the system without field monitoring or regulation, an additional field meter/controller unit such as the Lakeshore 475 DSP may be added for fine-control of the current/field and high resolution field readout. At the time of this thesis, the power supply has arrived but has yet to be tested. In addition, the recirculating chiller is scheduled to be relocated to a service shaft that is separated from the experiment by a concrete wall, to isolate the exhaust heat.
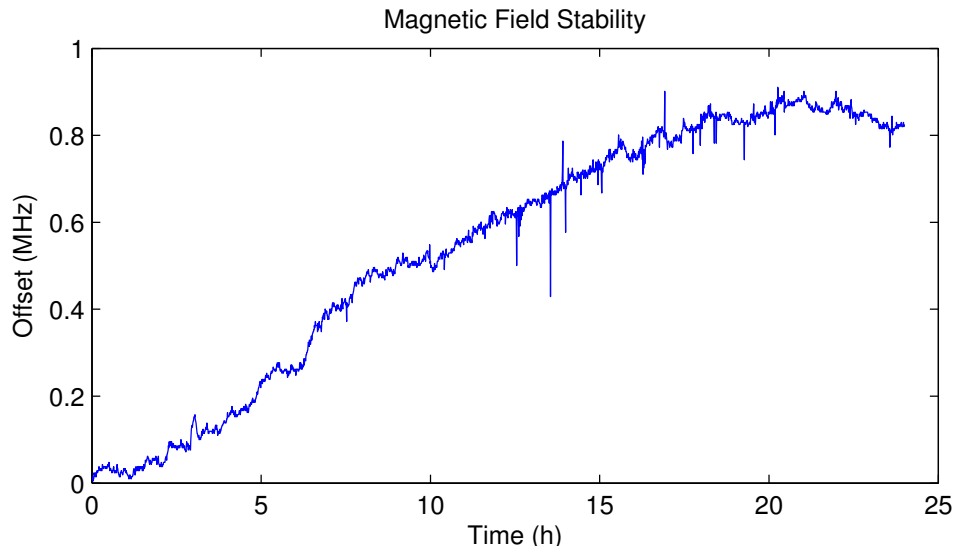
Figure 2.1: Field stability of the Varian Fieldial controller over a 24 hour period after startup, measured by tracking the resonance offset of an ESR sample in the magnetic field. Both long and short term fluctuations are observed. For an ESR frequency of roughly 10GHz, the expected 1ppm stability of the supply would correspond to 0.01MHz.

2.2   Pulse-Forming and Receiver Electronics

Our original, X-band, pulsed spectrometer design by C.A. Ryan, shown in Figure 2.2 was based on a first generation designs by J.S. Hodges[22], J. C. Yang [60] and D.G. Cory from MIT. The transmitting and receiving electronics follow a standard, superheterodyne architecture. Our design incorporated arbitrary phase modulation of pulses which was not included in the first generation MIT design but has since been proposed in a second generation design by M. O. Abutaleb [3]. Several additional improvements were implemented early in our spectrometer assembly and testing, resulting in the latter design, shown in Figure 2.3. Components are listed in Table 2.1. The sections of the spectrometer are now discussed in detail.

In both of our designs, A Rohde & Schwarz SMF100A microwave source with enhanced phase noise performance and high power output options generates high spectral purity microwave signals up to 22GHz and +23dBm, with 0.001Hz frequency setting resolution and phase noise of less than -65 dBc/Hz at a 10Hz offset and less than -115dB at 10kHz
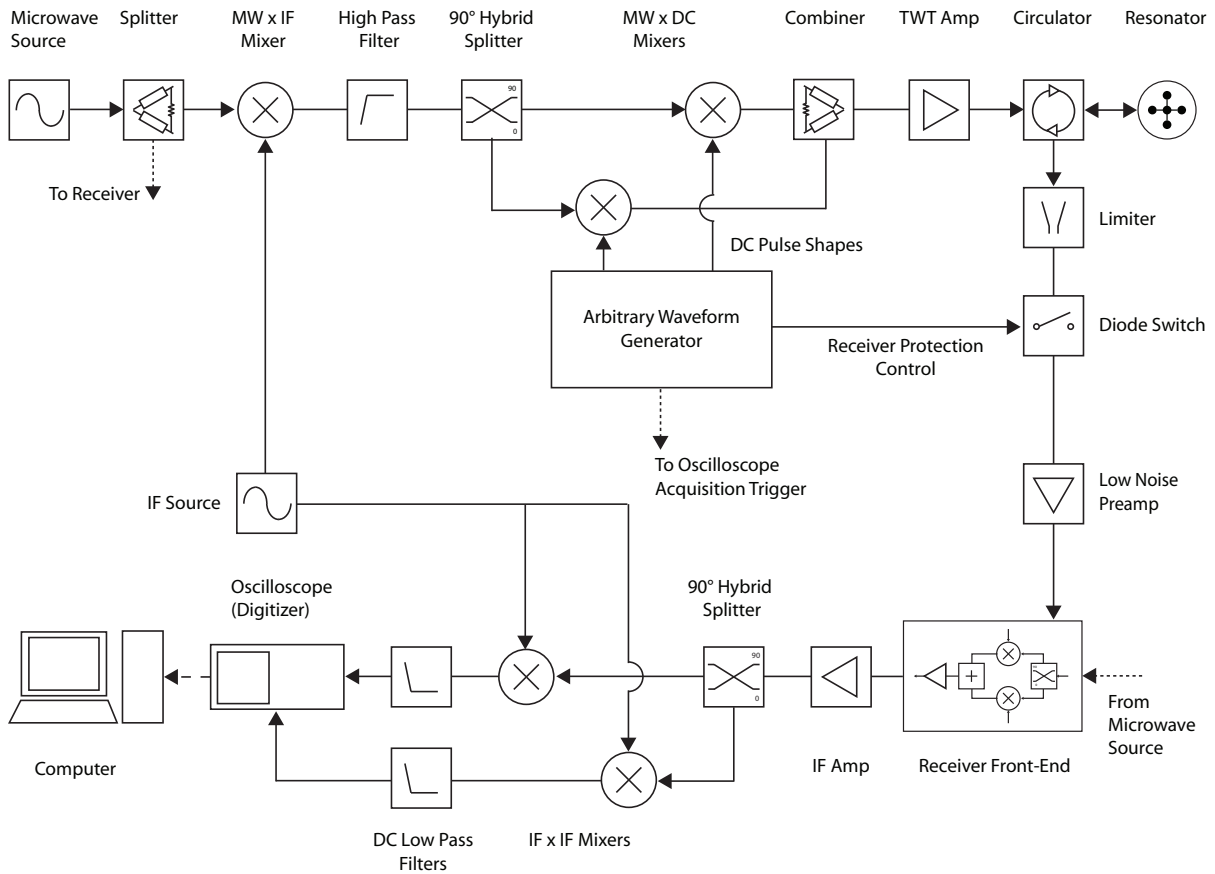
Figure 2.2: Early spectrometer design. Starting in the upper left corner, microwaves from a synthesizer are upconverted with an intermediate frequency (e.g. 200MHz) then split into quadratures. Each quadrature is amplitude modulated using microwave mixers and quasi-DC signals from two independent channels of an arbitrary waveform generator. The quadratures are recombined, amplified and directed to the resonator via a circulator. The receive-train is protected from high-power pulses by diode limiter and PIN diode switch. After pre-amplification, a receiver front-end mixes down and amplifies the signals for the intermediate frequency (IF) stage, where low-noise, economic IF amplifiers provide additional gain. The signal is mixed down again from the IF to quasi-DC for digitization. Several simplifications and improvements were soon incorporated into the design as shown Figure 2.3.

11
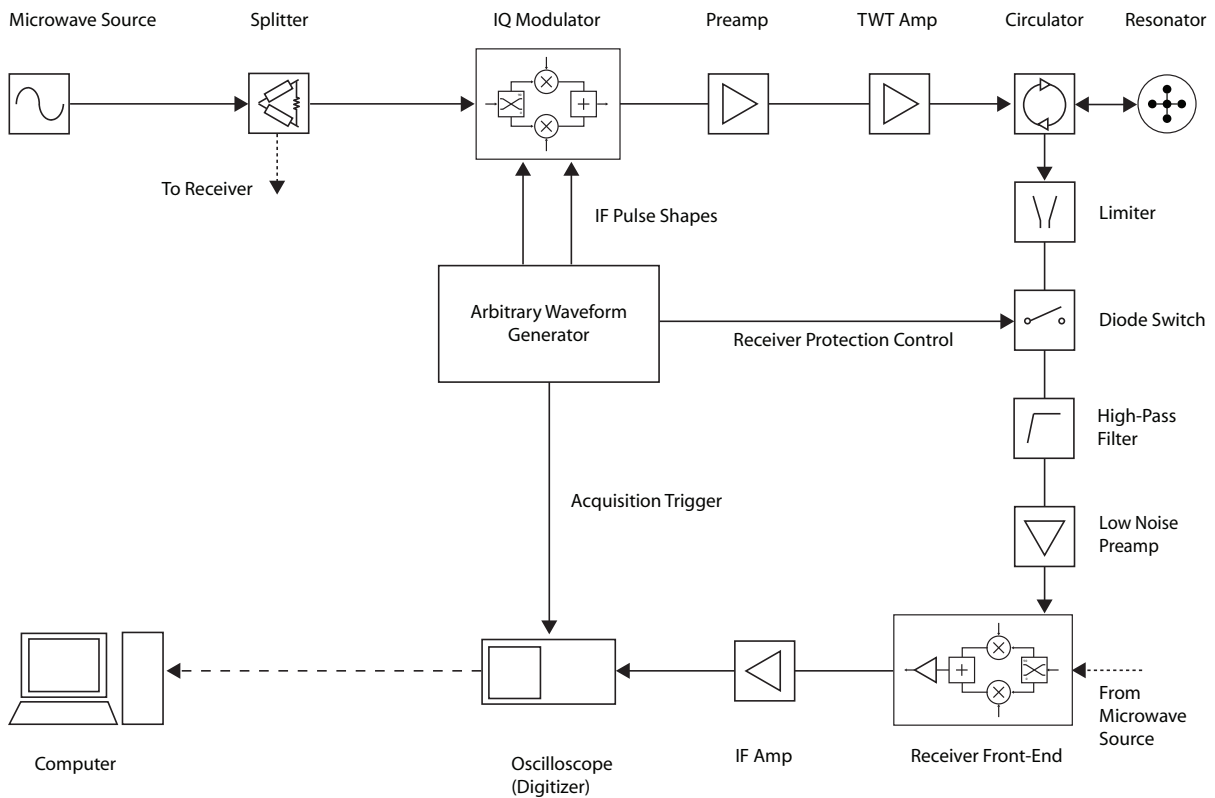
Figure 2.3: Later spectrometer design. Several improvements were made after initial tests of the first design, shown in 2.2. Using the 1GS/s fast sample rate of the AWG, the microwave pulse shapes are directly modulated at the 150MHz intermediate frequency, eliminating the need for an IF source and consolidating the IF and pulse-shape mixing and associated losses. The hardware is further simplified with an I-Q modulator package. A preamp has been added to exploit the maximum output of the TWT amplifier. In the receive-train, the fast sample rate of a 20GS/s oscilloscope digitizer is harnessed to directly digitize the signal at the IF, removing conversion losses from the IF-to-DC mix down stage.

Component	Manufacturer	Model
Microwave Source	Rohde & Schwarz	SMF100A
Splitter	Marki Microwave	PD-0220
I-Q Modulator	Marki Microwave	I-Q-0714LXP
AWG	Tektronix	AWG5014B
Preamp	MITEQ	AFS3-08001200-10-10P-4
TWT Amp	Applied Systems Engineering	117X
Circulator	DiTom Microwave	D3C8012
Limiter	Eclipse Microwave	EPL8012A3
Diode Switch	Advanced Technical Materials	S1517D
High-Pass Filter	Mini-Circuits	VHF-7150+
Low Noise Amp	MITEQ	AMF-5F-08001200-09-10P
Receiver Front-End	MITEQ	ARM0812LC2C
IF Amp	MITEQ	AU-1466
Low Pass Filter	Mini-Circuits	VLFX-400
Oscilloscope	LeCroy	WavePro 715Zi
Microwave SPDT Switch	JFW	50S-1313+15-TTL-SMA
Variable Attenuator	Advanced Technical Materials	AF886-20
Termination	Advanced Technical Materials	T0516

Table 2.1: Pulse shaping and receiver electronics list for figure 2.3. Some components listed here are used but not shown in the figure for simplicity.

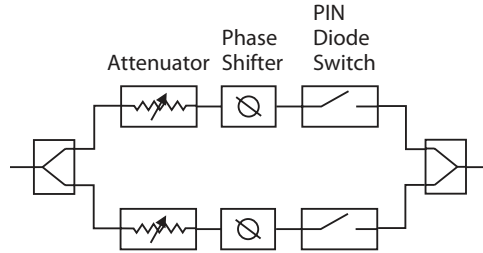Figure 2.4: Conventional spectrometer pulse forming architecture. A low-power, continuous microwave signal is applied from the left where it is split into different phase channels with a hybrid tee. Switches in each channel are opened and closed to form pulses. Using this technique, only square shaped pulses can be generated, and the phases are fixed during each experiment.

offset. The source utilizes an internal oven controlled crystal oscillator (OCXO) reference to ensure the utmost frequency stability.

2.2.1 Pulse Forming

Commercially available spectrometers typically generate pulses using a multiple-channel-switch method similar to that shown in Figure 2.4. Hybrid tees split a continuous signal into several phase channels, each with independent switches which are switched open and closed to form pulses of that phase. Only square pulses of a few, fixed phases can be generated with this design. Furthermore, each channel requires precise calibration of the phase shift and attenuation to achieve orthogonal, amplitude-balanced pulses for demanding experiments. In some designs, attenuators and phase shifters are provided, thus the relative amplitudes and phases are fixed upon manufacture and can not be adjusted. In these designs, typical phase errors of 1.5° have been reported [38]. Beyond the inconvenience of calibration, these restrictions prevent arbitrarily shaped pulses such as gaussians and optimal control pulses. They may also prevent composite pulses which require numerous, atypical pulse phases like the BB1[58] composite pulse. Fortunately these limitations can be easily avoided with current microwave technology.

In our original spectrometer design, the microwave carrier is first mixed-up with an intermediate frequency (IF) source, e.g. 150MHz, followed by a high-pass filter to reject the lower mixing sideband. The signal is then split into quadratures with a 90° hybrid
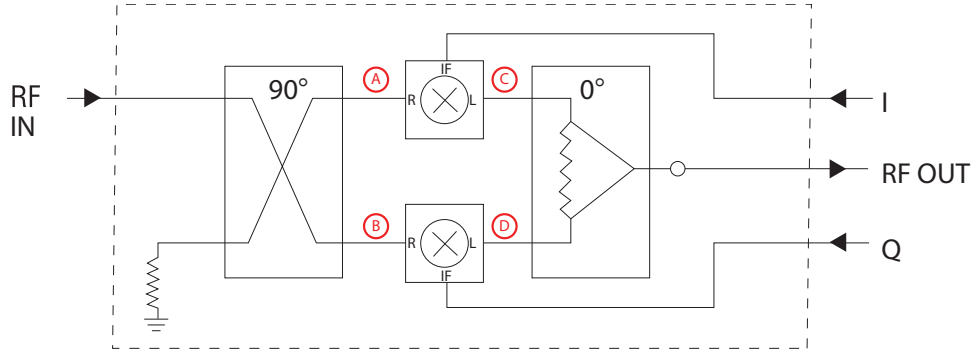
Figure 2.5: An I-Q modulator. By modulating at an intermediate frequency with phases carefully selected such that the Q port leads the I port, we perform single-sideband upconversion.

coupler. Each quadrature arm is modulated with arbitrarily shaped pulses generated by independent channels of a Tektronix AWG5014B 4-channel arbitrary waveform generator (AWG) which has 1ns time– and 14bit vertical– resolution. The quadrature signals are then recombined in a microwave power combiner. By controlling the amplitude relation ($\theta = arctan(\frac{Y}{X})$) between each signal quadrature, the phase can also be arbitrarily modulated at the time resolution of the AWG. This I-Q modulation scheme removes the need for separate phase-shifting components as in the MIT design which tend to have high insertion losses.

2.2.2 Single Sideband Upconversion & Phase Modulation

It was quickly noticed that the arbitrary waveform generator, with a sample rate of 1.2GS/s and output bandwidth greater than 250MHz was capable of generating an 150MHz intermediate frequency signal which is directly phase– and amplitude–modulated. Using two AWG channels to modulate both quadrature channels directly at the intermediate frequency, IF upconversion and pulse-shape mixing are consolidated into a single source. We further reduce the physical components by using an IQ-0714LXP Quadrature-IF double balanced mixer package from Marki Microwave, which supports intermediate frequencies from DC to 500MHz. The I-Q modulator block diagram shown in Figure 2.5.

By calculated use of the I and Q ports of the mixer, we suppress the undesired mixing sideband from the RF output without additional filtering. This technique is known as

single-sideband (SSB) upconversion. Referencing the figure, if we assume the RF IN waveform is of the form $\sin(\omega_0 t)$, then after the 90° hybrid coupler at point (A) the in-phase signal remains unchanged, and at point (B) we have the quadrature signal $\sin(\omega_0 t - \frac{\pi}{2})$. Meanwhile, we apply an intermediate frequency to the I and Q ports such that the phase of the Q port is leading the phase of the I port, i.e. we apply $\sin(\omega_1 t)$ to the Q port, and $\sin(\omega_1 t - \frac{\pi}{2})$ to the I port. Ignoring higher sidebands from the double balanced mixers, we have at point C,

$$
\begin{aligned}
A_0 \sin(\omega_0 t) \cdot A_1 \sin\left(\omega_1 t - \frac{\pi}{2}\right) &= \frac{A_0 A_1}{2}\left[\cos\left((\omega_0 - \omega_1)t + \frac{\pi}{2}\right) - \cos\left((\omega_0 + \omega_1)t - \frac{\pi}{2}\right)\right] \\
&= \frac{A_0 A_1}{2}\left[-\sin(\omega_0 - \omega_1)t - \sin(\omega_0 + \omega_1)t\right]
\end{aligned}
$$

and at point D,

$$
\begin{aligned}
A_0 \sin\left(\omega_0 t - \frac{\pi}{2}\right) \cdot A_1 \sin(\omega_1 t) &= \frac{A_0 A_1}{2}\left[\cos\left((\omega_0 - \omega_1)t - \frac{\pi}{2}\right) - \cos\left((\omega_0 + \omega_1)t - \frac{\pi}{2}\right)\right] \\
&= \frac{A_0 A_1}{2}\left[\sin(\omega_0 - \omega_1)t - \sin(\omega_0 + \omega_1)t\right]
\end{aligned}
$$

After the two signals are added in the power combiner, only the upper sideband, $A_0 A_1 \sin(\omega_0 + \omega_1)t$, remains at the RF OUT port, and the lower sideband is cancelled.

Microwave component packages called "single-sideband upconverters" apply the same technique, utilizing an additional 90° hybrid to supply the mixers with quadrature components of a single IF signal, requiring only a single IF input, thus a single AWG channel. We choose to use an I-Q modulator with independent I and Q inputs with two AWG channels such that the channels can be precisely calibrated to account for phase and amplitude imbalances in the IQ package, achieving optimal sideband cancellation at a particular microwave frequency.

Using our single-sideband upconversion technique, the output phase of the microwave pulse is precisely controlled by the phase of the intermediate frequency signal generated by the AWG, accurate up to its vertical resolution of 14bits (1 part in 16384). An additional benefit of mixing pulse shapes directly at the intermediate frequency is that inevitable,
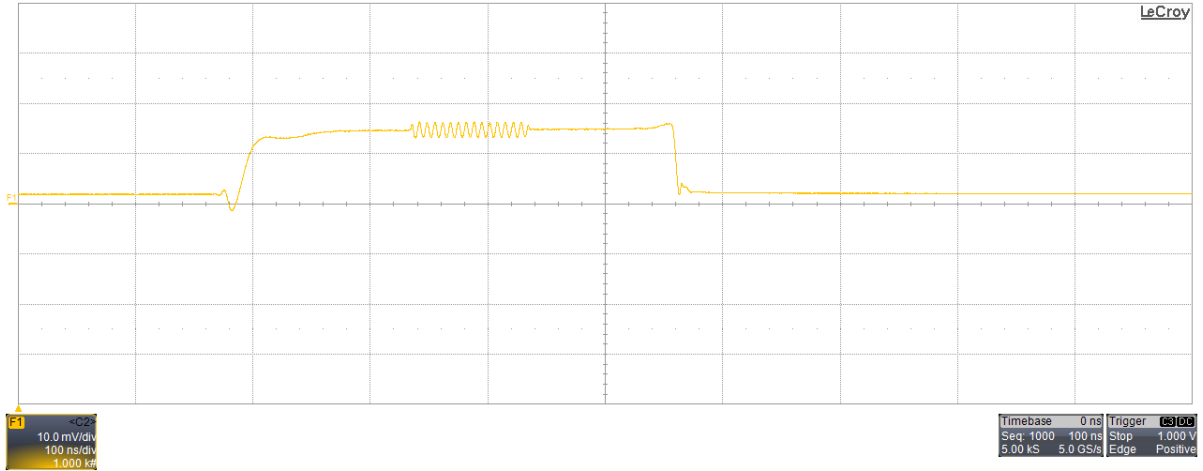
Figure 2.6: I-Q modulation off-resonant leakage. In this oscilloscope trace, a low-power 100ns pulse from the spectrometer has been downconverted to the intermediate frequency and recorded. The I-Q modulation leakage before, after, and throughout the pulse is amplified and detected in the receiver as a large DC offset. Since the power at this frequency is deliberately non-resonant with the spins, it has little effect.

unmodulated mixer leakage from the local oscillator to the RF output (LO-RF) will not be resonant with spins. In typical spectrometer operation, the microwave frequency is deliberately set 150MHz below the spin Larmor frequency. Only microwave power that has been upconverted to match the Larmor frequency will address the spins. Our I-Q mixer has a typical LO-RF isolation of 25dB, and is normally powered with a +13dBm RF input, meaning -12dBm can be expected to leak through the mixer regardless of the shape being applied to the IF ports. This small leakage will be amplified ($\sim$ 50dB) in subsequent stages, becoming quite significant. Having off-resonant leakage removes the need for further blanking-switches, and allows pulse shapes to utilize the full vertical range of power from maximum down to zero. The leakage is demonstrated in Figure 2.6.

Unfortunately, conversion losses in the I-Q mixer are high. The IQ-0714LXP mixer used had a conversion loss specification of 8dB maximum, however it was found to be much worse under our operating conditions. Using the high output power of our microwave source, we can drive the IQ modulator at the maximum of its specified power level (+10 to +13dBm). For the IF inputs, the specification point of 1dB compression (P1dB) is 4dBm, or 1.0 V_{pp}, which was also confirmed by measurement in Figure 2.7. Linearity of the pulse amplitude

17
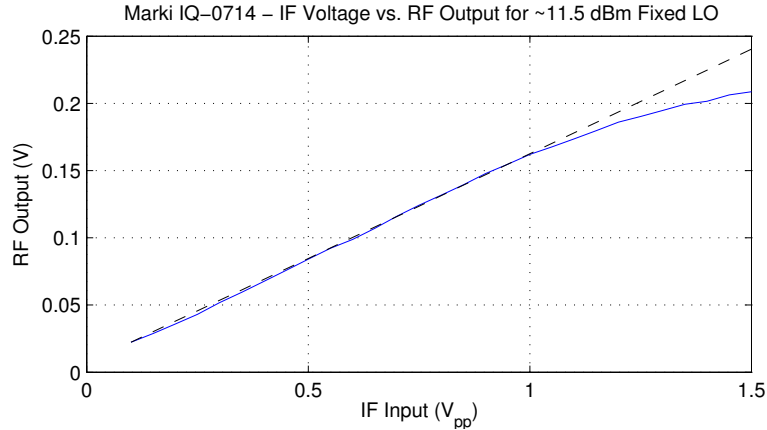
Figure 2.7: Experimentally measured I-Q modulator transfer curve at 10GHz RF and 150MHz IF frequencies, used in a SSB upconverter configuration.

is important for optimal control pulses, so we prefer to operate below the P1dB. It is likely that the conversion loss specification is for well beyond the P1dB, and for DC intermediate frequency. For the 150MHz upconversion used in the spectrometer, we observe a much greater conversion loss of about 17dB, as measured with a frequency counter/power meter.

2.2.3 Amplification

The next step is significant amplification of the microwave pulses in order to achieve fast nutation rates in the sample. We improve on the 12W amplifier in the first generation MIT design with a 1000W pulsed traveling wave tube (TWT) amplifier. The Applied Systems Engineering 117X TWT amplifier selected has a 1.5% duty cycle and $15\mu s$ maximum pulse length. At 10GHz it has maximum output of about 60dBm (1000W) with a gain of about 53dB at maximum output.

Due to the aforementioned conversion losses in the I-Q modulation stage, we first amplify the pulses using a solid-state pre-amplifier to fully utilize the TWT output range. Since we have an I-Q maximum output of roughly -4dBm, and a TWTA desired maximum input of +7dBm, an 11dB gain amplifier would be appropriate. We currently use a MITEQ AFS3-08001200-10-10P-4 low-noise amplifier, which has a 10dB P1dB and 26dB gain minimum. The gain is more than necessary for this stage, so an ATM AF886-20

ASE 117X TWT Amplifier Transfer Curve at 9.5GHz

X: –9
Y: 60.13

X: –2
Y: 61.17

Figure 2.8: TWT amplifier transfer curve with an arbitrary x-axis scale defined by the spectrometer. Using the manufacturer testing d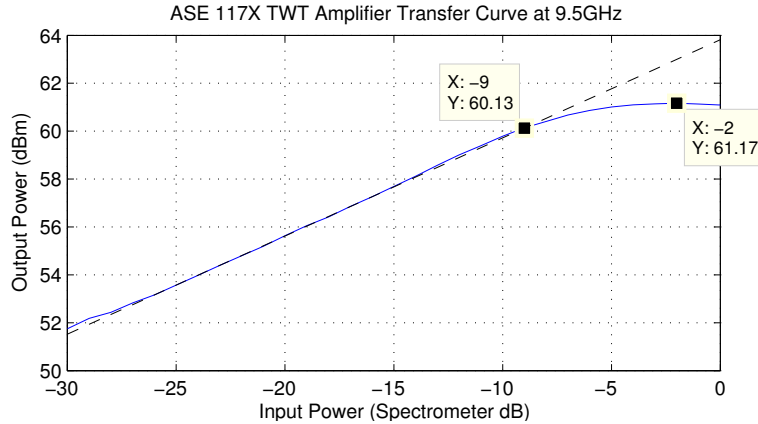ocuments of the TWT amplifier, the maximum output at a particular frequency can be estimated and the data points vertically shifted to match as has been done here. Once the vertical scale is established, the maximum spectrometer pulse power can be tuned using this plot and a variable attenuator to avoid damaging successive components, if necessary.

variable attenuator is currently used to further attenuate the input signal to the pre-amp. A better solution will be to use some combination of lower gain pre-amplifier, lower I-Q RF power, and lower I-Q IF modulation amplitudes.

The attenuator does provide a convenient means to calibrate and reduce the maximum output power of spectrometer pulses. In our design, the pulse power is limited by the circulators that follow the TWT amplifier which serve to direct pulses to the resonator and ESR signals to the receiver using the common transmission line. We currently use DiTom D3C8012 circulators which have a peak power limit of 500W (57dBm). To ensure that we do not exceed the power handling capability of the circulators, we calibrate using the optional forward RF sample port on the 117X TWTA which is connected to an internal 50dB directional coupler. Temporarily bypassing the resonator, the sample port is connected through an isolator and 40dB of additional attenuation then directly into to the receiver. In this manner we can safely monitor the TWTA pulse output. The calibration experiment, shown in 2.8, generates and measures pulses of increasing power which effectively measure the TWTA transfer curve slightly beyond its saturation.

The maximum voltage at the receiver can be measured, and associated with maximum

19

power values provided by the TWTA manufacturer for various x-band frequencies, thus calibrating the vertical axis. The experiment can now be repeated, increasing attenuation (decreasing output) until the maximum output is reduced to a safe level (500W) for the circulators. The calibration must be repeated when the operating frequency of the spectrometer is changed, since the TWTA output varies with freqency from 1100–1900W over its 8–12GHz range. The circulators should be replaced with higher power models e.g. the Teledyne KW Microwave C-7S43U-30 1kW circulator, however the calibration procedure is still useful to ensure the TWTA is operating in its linear transfer regime.

Phase Droop

An unfortunate property of the pulsed TWT amplifier is the varying output phase of its pulses, known as *phase droop*. Our 117X unit has an added phase droop correction option, specially designed for ESR. With the phase droop correction option installed, the phase droop is reduced from over $50°$ to a maximum $10°$ over $8\mu s$, but has been measured measured to be over $25°$ across the maximum $15\mu s$ pulse duration, as shown in Figure 2.9. For high fidelity operations this droop must be corrected, which can be accomplished by *pulse-fixing*. By sampling the pulse sequence immediately after the TWTA, deviations from the intended pulse sequence can be detected and corrections to the sequence applied for subsequent application to the sample. Traditionally, pulse-fixing uses a receiving coil that is (temporarily) inserted in or near the resonator which corrects for all errors in the spectrometer, including transmission into the resonator. For correction of simple pulses, i.e. square or gaussian shapes, distortions caused by the resonator are not expected to be significant, and sampling the output of the amplifier should be sufficient for correction.

2.2.4   Duplexing

Next, the high power pulses are directed to the resonator using the same transmission line as the ESR signals use to return to the receiver, accomplished using microwave circulators. Circulators are non-reciprocal, ferrite microwave components which present low loss through adjacent ports in one direction, but high isolation in the other direction. Each DiTom 3-port circulator provides only 0.35–0.40dB insertion loss between circulating
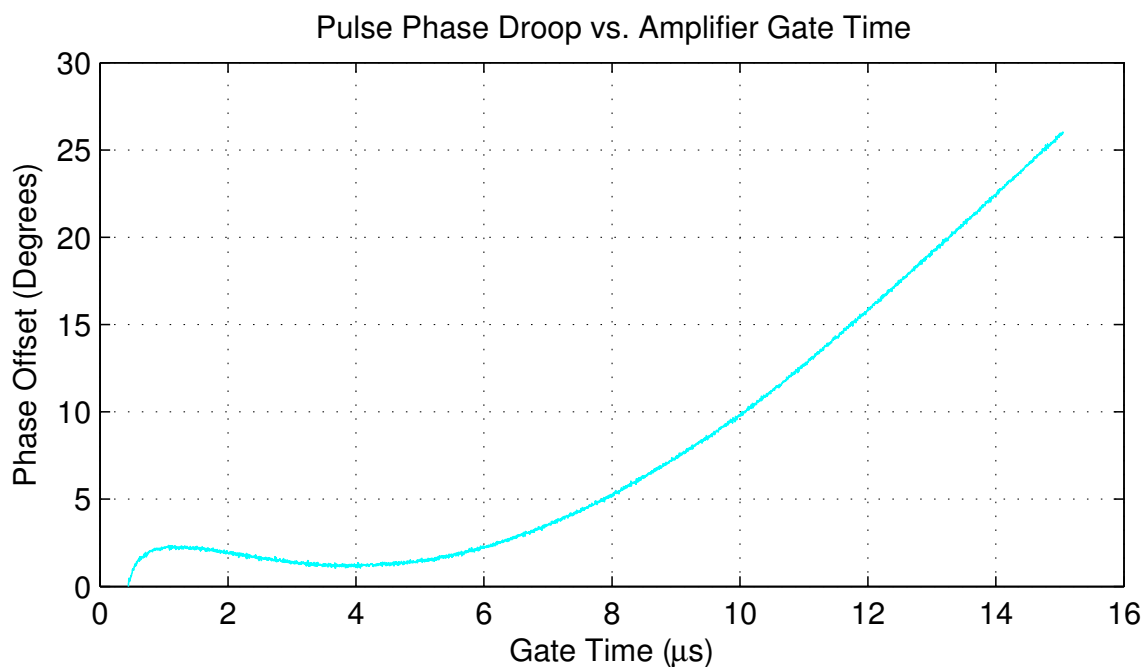
Figure 2.9: TWT amplifier measured phase droop. Using the amplifier's forward power sampling port, we measure a long microwave pulse directly to extract the phase droop over time.

Microwave Direction	Experience	Result	Typical	
Amp → Resonator	IL + IL	2×IL	0.7dB	
Amp → Receiver	IL + iso + IL	iso	22dB	
Resonator → Amp	iso + iso	2×iso	44dB	*
Resonator → Receiver	IL + IL	2×IL	0.7dB	
Receiver → Amp	iso + IL + iso	2×iso	44dB	*
Receiver → Resonator	iso + iso	2×iso	44dB	*

Table 2.2: Paths through a triple-junction circulator, referencing Figure 2.10. Typical values for insertion loss (IL) and isolation (Iso) are 0.35dB and 22dB respectively. Paths with an asterisk in the final column benefit from the cascaded-circulator architecture, namely a two-fold increase in isolation.

ports, but 20–22dB isolation between counter-circulating ports—typical values for octave-band microwave circulators. Since pulse powers may be up to 1000W (60dBm), increased isolation between components would be beneficial. The receiver will be protected by a power-limiter and a switch, both of which reflect microwave power. Power reflected from the receiver protection should be prevented from returning in the direction of the resonator and amplifier. Depending on the coupling to the resonator, significant microwave power may also be reflected from the resonator towards the amplifier. These problems can be reduced with a cascaded circulator approach [51].

Circulators which have one port terminated by a termination are called isolators, and thus the two other ports have low loss between them in only one direction. By chaining isolators and a circulator together, isolation between certain ports of the assembly are dramatically improved. As shown in Figure 2.10 and Table 2.2, by placing an isolator on the amplifier and receiver arms of the circulator, the isolation from resonator to amplifier; from receiver to amplifier; and from receiver to resonator are doubled. An associated penalty of doubled insertion loss from amplifier to resonator and from resonator to receiver is incurred—a small price for the increase in isolation. Indeed, more circulators may be cascaded in this way to further improve isolation at the sacrifice of insertion loss. X-band microwave circulators and isolators are also quite economical, costing about $200. Our spectrometer currently employs the triply cascaded circulator show in 2.10, although it is simplified in drawings for clarity. Unfortunately, isolation from the amplifier to the receiver can not be improved by cascading, and must be dealt with in subsequent stages.
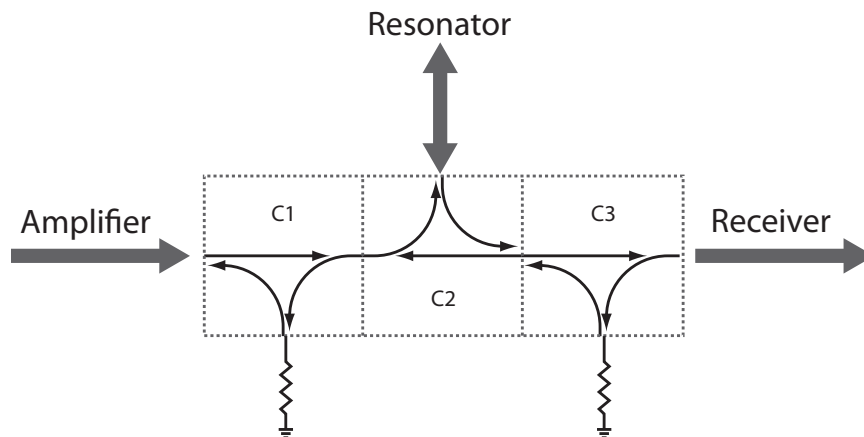
Figure 2.10: Cascaded circulators duplexing the resonator between amplifier and receiver. C1, C2 and C3 may be individually packaged circulators or a triple-junction circulator in a single package. Table 2.2 details the resulting isolation and insertion loss between paths.

2.2.5 Receiver

The receive-train of the spectrometer is responsible for amplifying the very weak ESR signals (nW – μW) and reduce the carrier frequency so that they may be readily digitized.

As previously mentioned, high power pulses from circulator leakage and resonator reflection will unavoidably enter the receiver and must be prevented from damaging the sensitive components. Since the receiver does not need to operate during pulses, a microwave switch can be used to isolate it from the transmitter. An ATM Microwave S1517D single-pole single-throw (SPST), reflective TTL switch provides 80dB of receiver isolation when open with a penalty of 2.5dB insertion loss. The S1517D has a fast switching speed of 20ns (from 50% TTL pulse to 90% or 10% RF) which ensures the receiver can be opened quickly to detect fast ESR signals after pulsing has finished. To control the switching, we use one of eight available 'marker' channels from our arbitrary waveform generator which also have 1ns timing resolution, but with only high/low amplitude output. Unfortunately, fast switches have been found to be very sensitive to high microwave powers, particularly when hot-switching. The S1517D has power restrictions of +10dBm continuous wave (CW) power for specification compliance, +30dBm CW survival, and peak 75W (+49dBm) for 1μs. Although the residual pulse leakage power is not expected to exceed these ratings, the switches are expensive—on the order of $1000—thus we provide additional protection
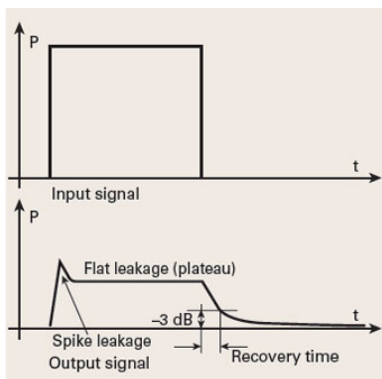
Figure 2.11: Diode limiter operation and terminology. Not shown are the limiting threshold which is the diode point of 1dB compression of a CW input, and the maximum leakage which is the CW point of full compression of the diode.

on the input in the form of a diode limiter, model EPL8012A3 from Eclipse Microwave. It has a 100W (50dBm) peak power handling capability, +12dBm limiting threshold (P1dB), +20dBm maximum leakage and 10–20ns recovery time, with an insertion loss of 1.5dB (see Figure 2.11 for definitions). The cost of diode limiters is on the order of $200, providing an economical safeguard for our expensive and sensitive diode switches.

Next we incorporate a high-pass filter, following Sturgeon et al. [52], to remove IF transients caused by the switch which are readily transmitted on the coaxial line. The MiniCircuits VHF-7150 high pass filter provides 30-60dB insertion loss to signals below 5GHz while an insertion loss of only 0.7dB at 10GHz, effectively filtering any transients at our 150MHz intermediate frequency as demonstrated in 2.12.

After the protection stages, the remaining signal should be the weak, ESR signals transmitted from the sample which must be amplified for digitization. As in the MIT design, we incorporate roughly 100dB of gain in multiple stages. The first stage is a MITEQ AMF-5F-08001200-09-10P low noise amplifier, providing a 42dB gain with only a 0.9dB noise figure. In the next stage, a receiver front end package downconverts the signals from microwave to the 150MHz intermediate frequency by mixing with a signal split from the microwave signal generator. The receiver front end uses image cancelation (single sideband) mixing analogous to our IQ modulator to remove the image frequency. The front end also includes 30dB of low-noise IF amplification, with the complete package having a noise figure of 2dB. Amplitude and phase imbalances make the image cancellation
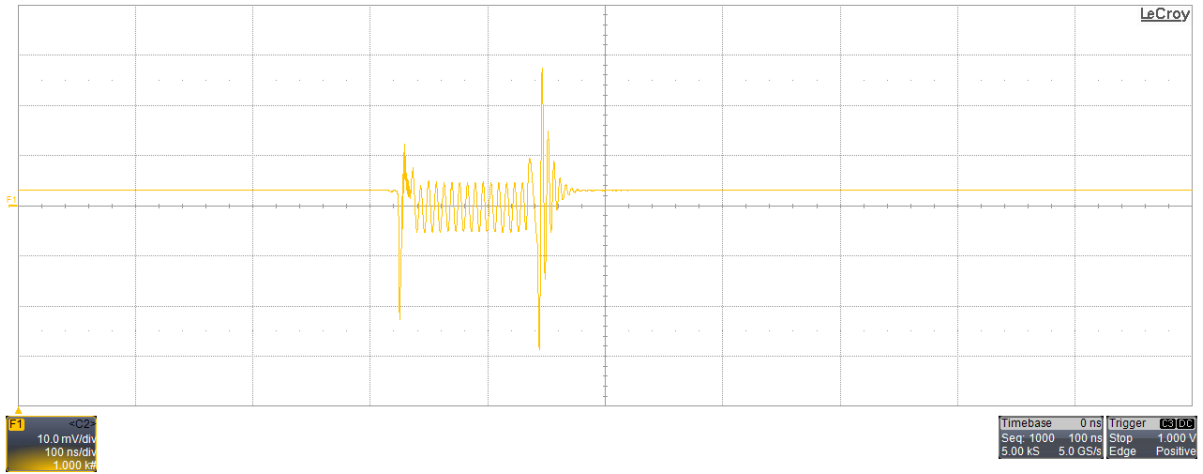
(a)
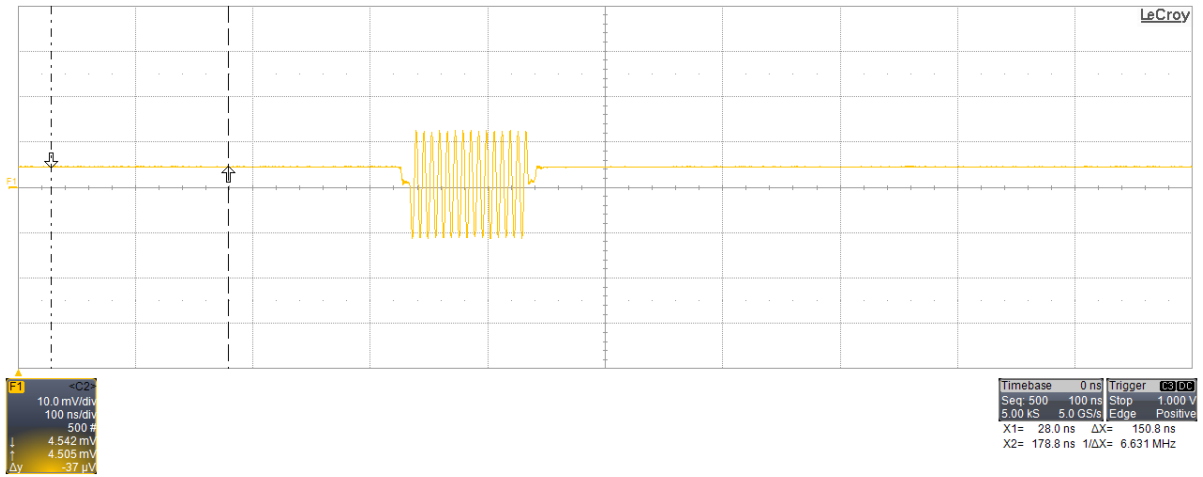
(b)

Figure 2.12: Oscilloscope traces of IF switch transients. In this experiment, a diode switch was tested as a blanking switch for mixer leakage, i.e. the switch was closed immediately before a pulse and opened immediately after. In (a), large transient signals from switching are observed before and after the pulse. In (b), a high pass filter after the switch attenuates the IF transients.

architecture somewhat narrowband, this package having a limited IF bandwidth from 100-200MHz.

The final step is to digitize the signal so that it may be recorded by the computer, and signal processed by Fourier transforming, integration etc. The latest design digitizes directly at the 150MHz intermediate frequency using a LeCroy WavePro 715Zi oscilloscope. The oscilloscope can sample up to 20GS/s with 8 bit resolution and has a 1.5GHz analog bandwidth. The oscilloscope can also perform signal-averaging on-board by recording a number of scans in "sequence mode," then averaging the scans. Once thethe desired number of scans have been sequenced and averaged, they can be transferred to the computer running the custom-made MATLAB spectrometer software, using a GPIB or ethernet connection.

2.3 Results

We have constructed an X-band (10GHz) ESR spectrometer designed specifically Quantum Information Processing. Our ESR QIP spectrometer boasts features such as

- Ultra stable microwave source with 0.001Hz resolution and less than -115 dBc/Hz phase noise @ 10kHz offset

- Current-stabilized electromagnet power supply with < 0.1ppm current drift over 30 minutes

- Pulse modulation at the intermediate frequency for precision phase control

- Digital demodulation at the intermediate frequency for precise receiver phasing

- 1ns timing resolution, 250MHz bandwidth and 14bit vertical resolution amplitude/phase shaping of pulses

- Custom built software interface provides experimental flexibility

2.4 Future Work

As experiments on the system ramp-up, an ongoing balancing act occurs between the importance of completing scientific research, and the merits of hardware and software improvements to the system which may interfere. A few potential improvements to the spectrometer could still be made, including:

- An internal digitizing computer card with on-board signal processing, as the second generation MIT design also proposes. The *Agilent U1084* or *Signatec PX1500* would be able to average signals much quicker that the current oscilloscope using hardware resources, and would eliminate transfer delays between a separate digitizing unit and the main computer.

- Higher power microwave circulators would allow transmitting the maximum TWTA power to the resonator.

- Consider higher intermediate frequency for lower noise as in the second generation MIT design

- Integrated resonator tuning with calibration functionality will allow us to check resonance frequencies without an external network analyzer.

- Software and interface improvements for better user experience and faster processing

Chapter 3

Resonator and Variable Temperature Probe

3.1 Resonator

In an ESR spectrometer, the resonator surrounds the paramagnetic sample and resonates on or near the Larmor frequency of the spins in the external field field. This resonance provides an enhancement to both the generated microwave pulses, and the detected weak spin signals. The loop-gap resonators is a type of lumped-element resonator in which the inductance consists of physically identifiable loops and the capacitance is made of gaps. Compared to cavity resonators, loop-gap resonators have large filling factors, large B_1 per square root watt, good B_1 uniformity, lower Q, larger bandwidths and shorter ringdown times [46]. Our group has experimented with a 2-loop-1-gap resonator, adapted from[15], and a 5-loop-4-gap "rising-sun" resonator adapted from [45] and shown in 3.1.

The rising-sun resonator has 5 loops and 4 gaps arranged symmetrically about a central sample loop. The symmetric arrangement should improve RF homogeneity over a 2-loop, 1-gap geometry. The resonator and shield are machined from a solid rod of oxygen-free high-conductivity (OFHC) copper. A copper prototype was chosen for quick turn-around machining, however the resonator would ideally be made of silver-plated ceramic, allowing external modulation fields to penetrate for continuous wave ESR or electron-nuclear double resonance (ENDOR). The loop (2.5mm) and gap (0.2mm x 1.2mm) dimensions are quite
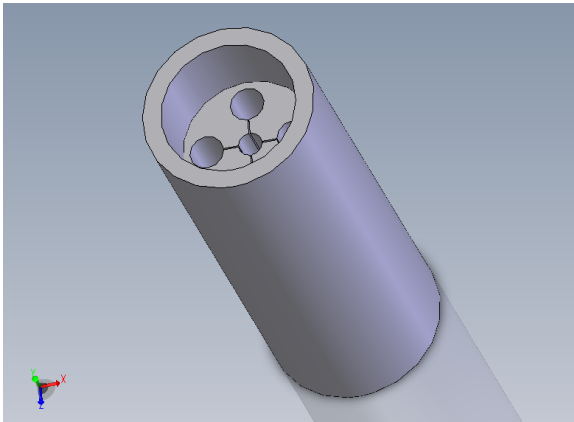
(a)
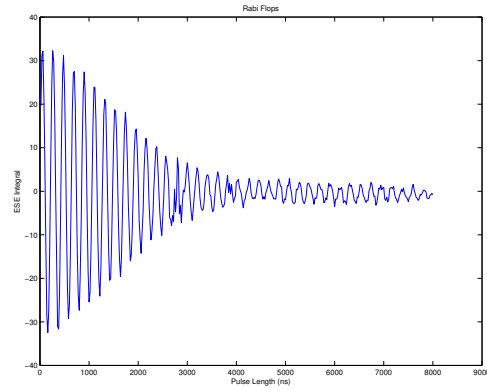
(b)
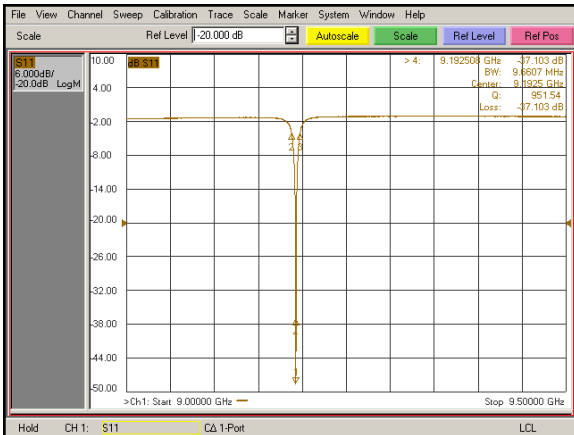
(c)
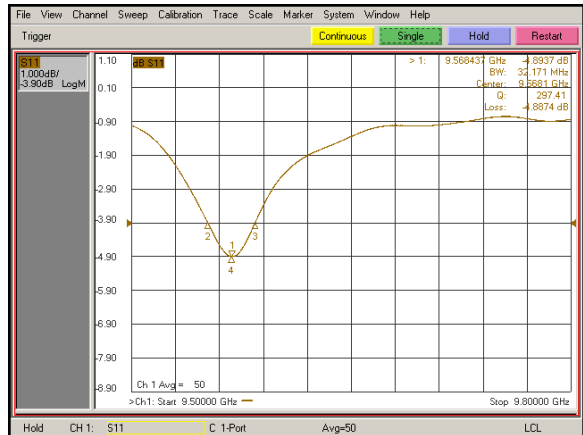
(d)

Figure 3.1: (a) Rising-sun resonator with shield, made of a single piece of OFHC copper. (b) Long Rabi oscillations measured with the resonator to 8μs (unfortunately magnetic field fluctuations caused the signal spikes). (c) a critically-coupled resonator trace showing Q$\sim$1000. (d) an over-coupled resonator trace showing Q$\sim$300.

small and require high tolerances for a predictable resonance frequency. Electrical-discharge machining (EDM) is a technique of removing material by rapid current discharges, and can create features of dimension 0.003 inches (0.0762mm) with tolerances of +/- .0001". In our experience, care must still be taken with EDM to ensure a working finished-product. One resonator prototype had metal burrs remaining in the gaps which caused very erratic behavior. Our best resonator was first pre-drilled, the gaps were rough cut with 0.004" EDM wire, and finally a low-power finishing cut was done which removes very slight amounts of material to gain finish and precision. This work was done by Protechnique EDM, Milton, Ontario. The finished resonator unloaded frequency was found to be about 9.7GHz.

Coupling to the resonator by the transmission line is the inductive type, achieved by positioning a loop of the coax conductor (soldered to its shield) directly above an outer loop of the resonator. Impedance matching is varied by moving the coupling loop towards and away from the resonator, providing a large coupling range as shown in 3.1(d). For pulsed ESR experiments, a low quality factor (Q) is desirable as ringing of the resonator after a pulse interferes with detection of short-lived ESR signals. The ringdown time constant is related to Q by $\tau = Q/2\pi f_0$, where f_0 is the resonant frequency. In addition, mulitple-qubit ESR spectra can be fairly broad thus a large resonator detection bandwidth ($\Delta f = f_0/Q$) is desired. For a resonator frequency of 10GHz and bandwidth of 100MHz, a Q as low as 100 is required. However there is a tradeoff as lower Q translates to lower ESR signal. Spoiling the resonator Q can be accomplished by constructing intentionally lossy resonators using lower-conductivity materials and lossy dielectrics in the gaps, or it may be achieved by overcoupling. Rinard et al. [45] have shown that it is better to construct the resonator with the highest Q possible, using high-conductivity materials and overcouple it to achieve low Q. For resonators spoiled to the same Q by the two methods, they show that the overcoupled resonator may yield up to $\sqrt{2}$ times the signal voltage of the inherently low Q resonator.

3.2 Variable Temperature Probe

In ESR experiments, varying the temperature of the sample can be extremely desirable. One reason is the polarization of electron spins ($tanh\frac{h\nu}{2kT}$) may be improved by lowering
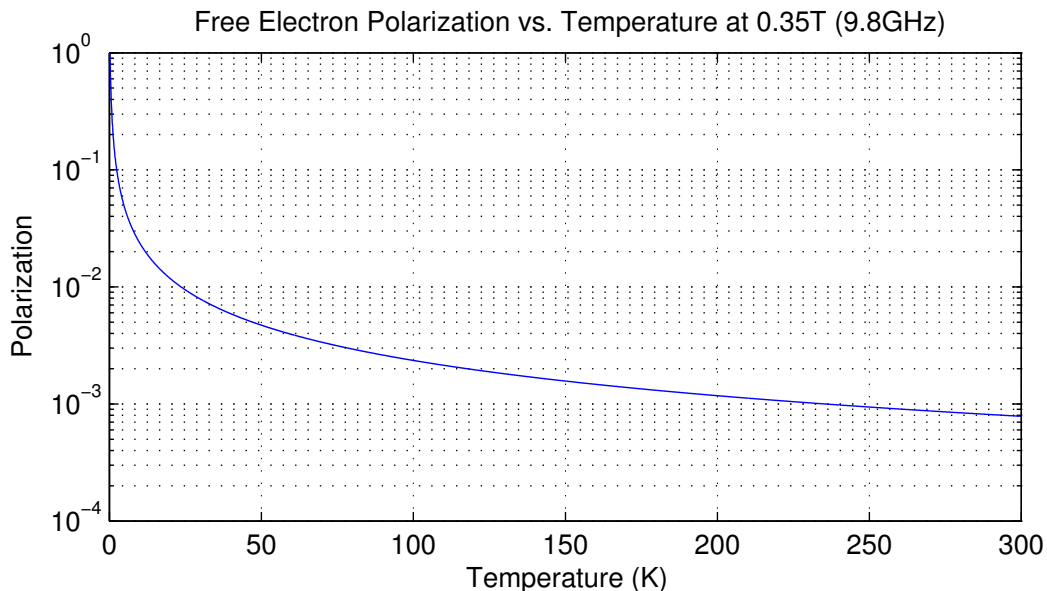
Figure 3.2: Electron spin polarization as a function of temperature. Three values are highlighted at the 1atm boiling points of helium and nitrogen and at standard room temperature.

the temperature, as shown in Figure 3.2. At X-band frequencies, decreasing the sample temperature from 300 to 77K results in roughly 4 times better polarization, while 4.2K gives almost 70 times the polarization of room temperature. To lower the temperature of ESR samples, probes must be designed which provide for the usual ESR requirements and also interface with a cryostat. The probe and cryostat arrangement must conduct heat from the sample to a cryogenic bath, either by immersing the sample directly in cryogen or through mutual contact with a thermally conductive material which separates the two.

3.2.1 Cryostats

Our group has experimented with two types of cryostats and associated probes: a modified reservoir type cryostat, and a continuous-flow type cryostat, both depicted in figure 3.3.

NOTE: ALL DIMENSIONS ARE IN INCHES.

2.0 O.D. HELIUM RESERVOIR PUMPING ARM

THERMAL ANCHOR
EVACUATION VALVE

3.0 O.D.
6.0 O.D.
10.0 O.D.

HELIUM RESERVOIR
NITROGEN RESERVOIR
CHARCOAL GETTER
FUNNEL GUIDE

3.5 O.D. VACUUM SHROUD
3.25 O.D. RADIATION SHIELD
2.75 O.D. SAMPLE TUBE

4.0
24.0
USER SPECIFIED
2.96
1.5

473 mm
351 mm
125 mm
170 mm
125 mm
95 mm
43.7 mm
55 mm

Exhaust capillary
Cryogen flow access
Inlet capillary
Heat exchanger
5mm clear window
Sample centre line
Blow-off valve
Vacuum valve
Transfer tube entry arm

(a)   (b)

Figure 3.3: (a) a Janis Research Company CDNT-NMR reservoir-type cryostat. In the reservoir modifications described, the bottoms of all three layers are removed. The inner, cryogen-space bottom is replaced with an oxygen-free, high thermal conductivity copper cylindrical block called the cold finger. The nitrogen-contacted radiation shield remains open at the bottom, and the outer vacuum shroud is sealed to a new vacuum box which contains the resonator and sample. Thermal contact must be provided between the sample and the copper cold finger. (b) an Oxford Instruments CF935O continuous-flow type cryostat. Note that this figure shows the reservoir cryostat in the upright, operating position, however the continuous-flow is shown in a horizontal orientation for labeling convenience by the manufacturer. In the continuous-flow, continuous-transfer type cryostat, an external supply of helium liquid is attached through a transfer tube into the entry arm, where it is connected to a capillary tube that reaches the sample space. The sample space is vacuum pumped, drawing helium through the system and immersing the sample in the flowing vapour. A continuous flow probe serves to position the resonator and sample near this helium flow.

32

Reservoir Cryostat

Reservoir-type cryostats are normally designed to immerse a sample directly in a cryogenic liquid. For cryogenic efficiency, a liquid helium reservoir is surrounded by several vacuum layers and a liquid nitrogen reservoir. The cryostat shown in figure 3.3(a) is designed specifically for NMR research, with a long "tail" to position the sample in a superconducting magnet. The helium space and thin vacuum chambers extend to the bottom of the tail, and a single-wall tube which is contacted to the nitrogen reservoir acts as a radiation shield. Thermally sunk to liquid nitrogen temperatures, the shield serves to minimize radiation losses ($\propto T^4$), while the vacuum spaces, when evacuated to $\sim 10^{-5}$ Torr reduce convective losses. Both the Cory group [22] at MIT, and Y. Zhang [61] and J. Baugh at IQC have modified NMR reservoir cryostats for EPR use.

The modifications to the tail proceed as follows: the bottom of the outer vacuum shroud is removed. The shroud tube is instead sealed to a vacuum box which is designed to accommodate an ESR resonator and fit between the poles of an electromagnet. The bottom of the nitrogen-contacted radiation shield is removed and remains open. The bottom of the helium space is replaced with a copper disk, called the cold-finger, which will ideally reach liquid helium temperatures on both the helium– and vacuum–facing sides. A sample holder that can bring the sample into thermal contact with the vacuum face of the cold-finger is then made. Reservoir cryostats have a large capacity for cryogens and are useful for maintaining samples at low temperature for extended periods of time. However, cooling down a reservoir cryostats is a long and involved process, and only a relatively small temperature window can be achieved (i.e. from ~4K to 1K with helium by evaporative cooling). In addition, both research groups have struggled to actually reach liquid helium temperatures at the sample, attributed to problems from thermal contractions in the designs.

Using the modified reservoir cryostat and probe at IQC, two different techniques to estimate the sample temperature were used by Zhang and Baugh. The first, using liquid helium cryogen, involved measuring the T_2 relaxation time of a crystal of chromium doped potassium perchromate ($Cr:K_3NbO_8$), as shown in 3.4. The temperature of the coldfinger was monitored by a temperature sensor and momentarily reached 6K but was not stable and shortly began to rise. The measurements were taken at approximately 18K coldfinger
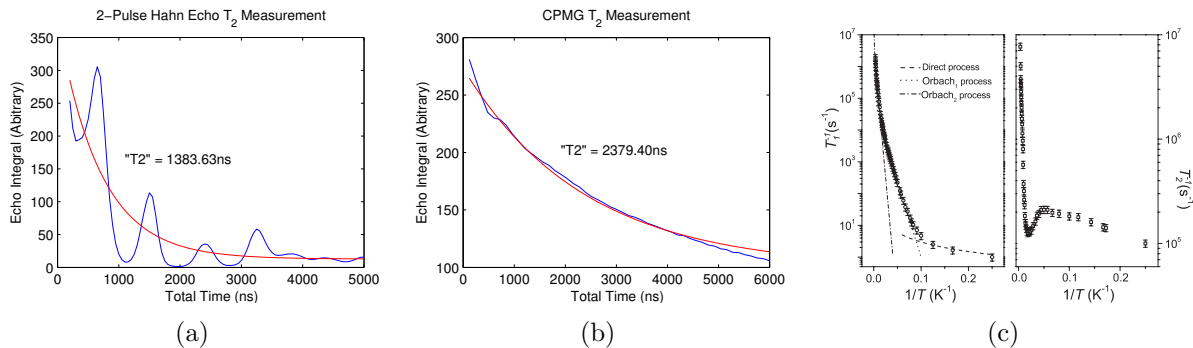
Figure 3.4: Cr:K_3NbO_8 temperature measurements with the modified reservoir cryostat, coldfinger temperature measured to be roughly 18K. (a) A 2-pulse Hahn echo T_2 measurement. (b) CMPG T_2 measurement at 18K. (c) T_1 (left) and T_2 (right) published relaxation data from Nellutla et al. [41]. The local maximum T_2 of 8μs occurs at roughly 50K, indicating that the sample temperature in these experiments was well over 50K.

temperature, and gave a T_2 relaxation time of 1.4–2.4μs. From the data published by Nellutla et al. [41], this corresponds to a temperature well over 50K (the local T_2 maximum shown in 3.4(c)).

In another experiment using liquid nitrogen cryogen, shown in Figure 3.5, field-swept signal intensities were compared to room temperatures. In a field-swept echo experiment, each point represents the integral of a spin-echo experiment, taken as the field is swept. ESR signal is proportional to sample polarization, thus comparing the signal intensities gives a course estimate of sample temperature (changes in relaxation rates will also affect the echo integral). The ratio of peak heights at room temperature and at the coldfinger temperature of 77K was measured to be 2.6, implying a sample temperature of 113K, 36K above the coldfinger.

Despite the temperature problems, positioning the sample in vacuum may be necessary for loop gap resonators due to the potential for arching in the presence of helium gas. Several improvements to the reservoir cryostat are possible which may help achieve a lower, stable sample temperature. The radiation shield which was removed due to suspected contact with outer shields should be used. The shield should be pre-cooled by the outer nitrogen reservoir for some time before helium cool-down. In addition, radiation shield(s) contacted to nitrogen and/or helium baths which extend around the resonator and sample may be beneficial [30]. A simple electronic-less probe for the helium reservoir with baffles at
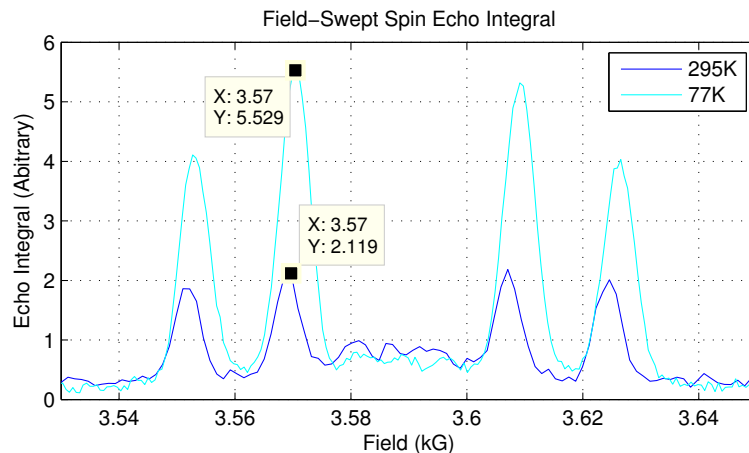
Figure 3.5: Labelled malonic acid field-swept signal in reservoir probe at 300K and 77K coldfinger temperatures. Signal intensity is proportional to the sample polarization, thus by comparing peak heights we can estimate the sample temperature was 113K, a difference of 36K.

several positions in the tail and upper reservoir would reduce radiative losses and encourage evaporating gas to cool the dewar walls [30].

Continuous Flow Cryostat

Continuous-flow type cryostats use vacuum pressure to continuously draw a small amount of cryogenic liquid through a capillary tube, and vaporize it before flowing directly on to the sample holder. A needle valve is used to control the flow rate, while a variable heater near the outlet of the cryogen adjusts the temperature of the exiting vapour. Automated temperature controllers continuously adjust the valve and heater to achieve stable temperatures in the range of 1.5 - 300K. Samples may be either directly immersed in the flowing vapour (cryostat used herein), or separated from the flow by a cold-finger which maintains thermal contact, leaving the sample in vacuum. With the sample in vapour, both the sample and holder are readily cooled, removing the need for challenging thermal anchoring, and since the sample is not in a highly evacuated space, it may be easily and quickly rotated or even changed. Having the sample cooled by a cold finger makes access to the sample more difficult, however it may be isolated from vibrations which may be caused by flowing vapour. One consideration of continuous flow cryostats and probes is the presence

of helium gas, which has a low breakdown voltage and may lead to arcing in small gaps of a pulsed resonator structure.

In addition to added polarization, the relaxation rates of many samples are strongly temperature dependent, several of which have relaxation rates too short to be even detected at room temperature. However, certain samples may have relaxation rates that may be inconvenient for experimentation at lower, fixed cryogen temperatures. The T_1 relaxation of phosphorous donors in isotopically purified silicon (Si:P), for example, varies by 5 orders of magnitude from 20–7K, increasing to roughly 0.1s [55]. Due to the weak signals involved, ESR experiments usually require signal averaging—the repeated addition of signals from identical experiments, potentially hundreds or thousands of times. During signal-averaging the same initial state is required for each experiment, thus the system must be left to completely relax between experiments. The usual rule of thumb is to delay for a period of 5 times the sample T_1. In the case of Si:P at 7K, this would mean nearly 10 minutes of delays per thousand averages, and even longer at 4.2K or lower.

Still other samples may not be compatible with fixed cryogen temperatures whatsoever. $N@C_{60}$ dissolved in CS_2 solution is a useful sample for ESR QIP[39, 6, 20], and is used for studies discussed in Chapter 4. The T_1 and T_2 relaxation times decrease exponentially from $120\mu s$ and $80\mu s$ respectively at room temperature to roughly $400\mu s$ and $250\mu s$ at 170K. However, below 160K the CS_2 solvent freezes, causing regions of high fullerene concentration around polycrystal grain boundaries, and T_2 relaxation to become extremely short due to dipolar coupling [39].

In addition, the ESR spectroscopy community has standardized around quartz sample tubes, 4mm outer diameter and 3mm inner diameter, between 10 and 25cm long (see, for example Wilmad Labglass, or Norell Inc.). Sample tubes of these dimensions are most readily accommodated in continuous flow cryostat probes with the sample tube (and sample) directly cooled by the flowing vapour.

For these reasons an ESR probe was also designed for an existing Oxford Instruments Spectrostat NMR 86/62 continuous-flow cryostat, previously used for NMR studies in a superconducting magnet. The cryostat is shown in figure 3.3(b). The low-temperature system consists of an ITC503 temperature controller, a GF4 oil-free vane pump and a LLT650/10 low-loss, automated liquid helium transfer line. The system provides a sample-

space diameter of 62mm, temperature stability of 0.1K, helium consumption of 1.3 l/hr and a cool-down time of 90 minutes from room temperature.

3.2.2 Spectrostat Probe

The probe design, shown in Figure 3.6 follows Isaacson et al. [25], but is also similar to the commercial Flexline probes from Bruker Biospin. A cryostat cap is machined from aluminum, which seals to the cryostat top flange with an o-ring and 3 screws. The cap has a 1/2" SwageLok Ultra-Torr o-ring fitting for the sample loading tube entry port, and a 1/4" fitting for the coaxial cable entry. The cryostat sample space is under light vacuum pressure ($\sim$0.1 Pa) from a continuously pumping mechanical pump, so the seal does not need to withstand high vacuum.

The cap has an additional assembly to allow for fine adjustment of the coupling resonator coupling via the Micro-coax UT-250A-M17 semi-rigid coaxial cable. The cable has a silver plated copper conductor, PTFE dielectric and a 0.250 inch diameter copper outer conductor, giving extremely low losses of 1.08 dB/m and an average CW power handling of 350W. The coax body is extremely rigid so the coupling motion may be translated from the cap through the length of the probe to the resonator. A threaded brass sleeve grips the coax shield with set screws, and a knurled aluminum knob threads onto the sleeve, but is held in a fixed position from the cryostat cap. Turning the knob forces the sleeve and coax to translate vertically, changing the coupling at the resonator. The transmission line has an SMA joint near the coupler which allows for the coupler to be removed, and calibration standards to be attached so that network analyzer calibration can be performed. Joints in the coax are not ideal since breaks in the PTFE dielectric allow it to migrate when thermally cycled. If air (or worse – helium) gaps are formed, arching in the transmission line could occur. Unfortunately, due to line resonances caused by the long length of coax, the joint was necessary to tune the coupler.

Cryogenic G10 is a glass cloth laminate impregnated and cured with a non-brominated epoxy resin. Its low thermal expansion and conductivity make it an ideal material for cryogenic applications. It is used extensively throughout the probe as it is straightforward to machine and joints do not require welding. G10 rod and tubes were obtained from Accurate Plastics Inc., Yonkers, NY.
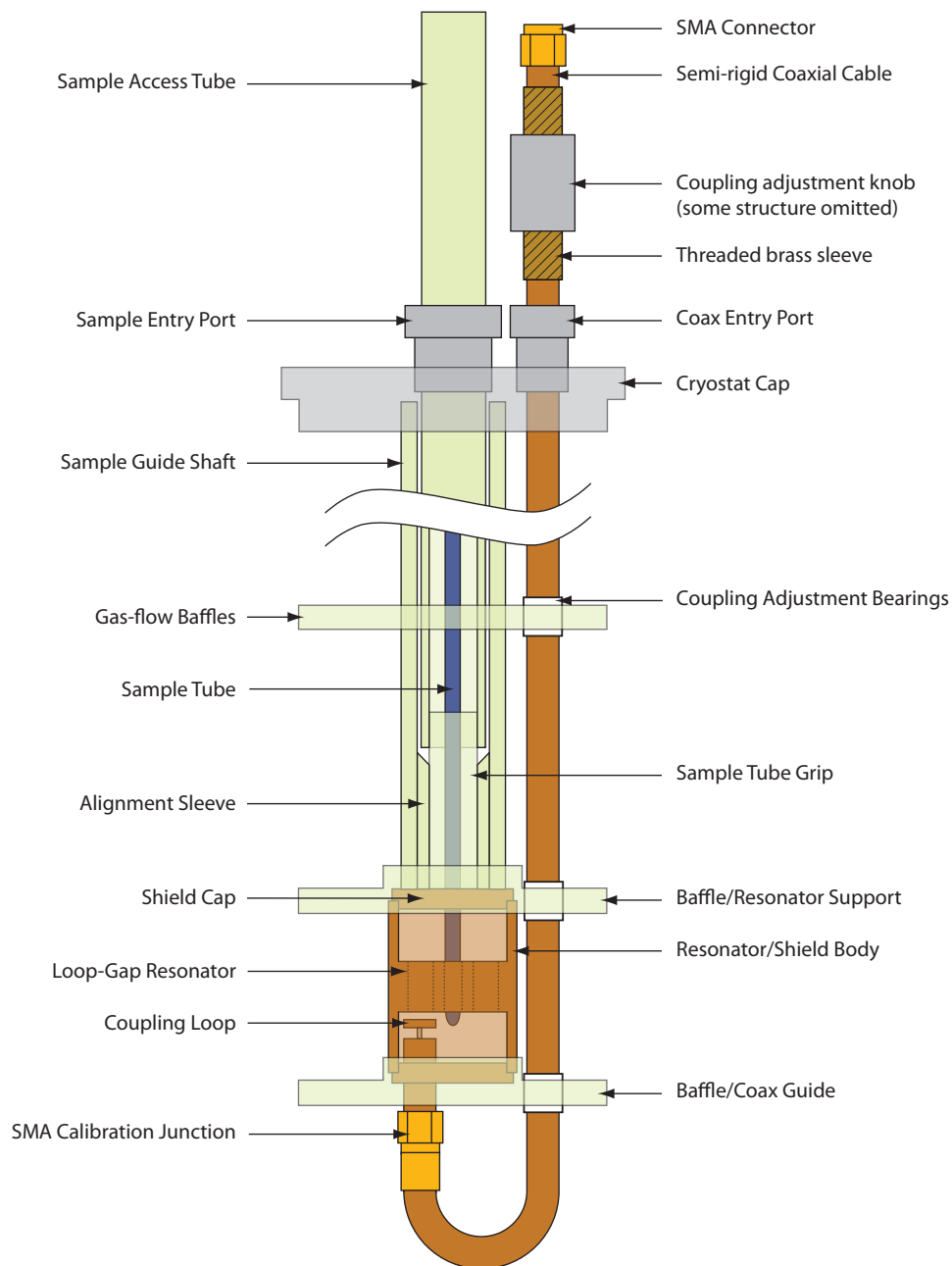
Figure 3.6: Custom-built ESR probe for Oxford SpectrostatNMR cryostat and loop-gap resonator. Designed for low temperature experiments near the bottom of large superconducting magnets, the cryostat requires a probe roughly 1m in length.

Threaded into the bottom of the cryostat cap is the sample guide shaft, made of G10 rod. The shaft guides the sample access tube, which has a specific outer diameter to seal with the entry port. The sample access tube is threaded at the bottom to mate with a short section of G10 rod which is only bored out enough to make a tight fit with a standard, 4mm quartz sample tube. A short section of narrower diameter G10 tube acts as an alignment guide for the sample grip as it nears the bottom of the guide shaft.

The guide shaft is aligned in the central axis of the cryostat by baffles machined from G10 sheet and epoxied to the shaft using 3M Scotch-Weld 2216 epoxy. As stated, G10 was used throughout for convenience, however metal baffles are preferable for thermal conductivity to reduce radiation. Each baffle has a split bearing machined from Teflon rod to allow for motion of the coaxial microwave line. The splits are necessary to accommodate considerable shrinkage of Teflon at low temperature. The second lowest baffle also serves to join the resonator shield body to the probe assembly, and hold shield cap in place. An inner thread on the baffle mates with an outer thread machined into the copper resonator shield. Similarly, the lowest baffle threads onto the resonator shield, and also serves to align the coaxial cable and coupler with the resonator.

3.2.3   Second Generation Probe

This probe has served as an acceptable prototype, however it has several shortcomings that could be fixed by a next-generation probe. Ideally, a new cryostat that is purpose-built for ESR should be used. The SpectrostatNMR cryostat is approximately 1m in length, much longer than is necessary to position a probe head outside of the 12" electromagnet poles. The Oxford CF935O cryostat, designed for ESR experiments, has a sample space that is a much more suitable 14" in length. However, the concerns of helium gas in a loop gap resonator need to be addressed. A Janis SuperTran continuous-flow, sample in vacuum cryostat may be more suitable.

The most important improvement would be to avoid the coupling-from-the-bottom, candy-cane type coaxial coupler. Due to asymmetries of the coupler, displacing the coupler causes the resonant frequency to shift. By fashioning the coupling loop out of a slice of the coaxial shield, it has good axial symmetry, and translating toward and away from the resonator does not change the frequency significantly. Holding it fixed in the other

directions while allowing translation is a challenge, and indeed the current probe has some "wiggle," meaning the frequency can shift after disconnecting a network analyzer at the probe head, for example. In addition, the bend increases the length of the coax and is difficult to bend precisely to align with an outer resonator loop. The bottom coupling arrangement also takes up space at the bottom of the cryostat, pushing the sample further from the heat exchanger. Coupling from the top, as in [45] is preferable. In the current design, coupling from the top is prevented by the large sample guide shaft and large coaxial cable diameter.

The dimensions of the guide shaft, and most of the G10 tubes can likely be reduced since it is stronger than was expected. 1/16" tube wall thickness was found to be more than adequate. In addition, thin-wall stainless steel tube could be used to save space. The o-ring seal fittings come in standard diameters, i.e. 1/4", 3/8", 1/2", thus one of the smaller sizes should be selected and the new guide shaft and sample loader chosen accordingly.

G10 baffles, planned to be quick-fabricating were actually quite time consuming since G10 is quite abrasive on tools. Metal baffles should be used for better radiation shielding.

Chapter 4

Benchmarking the ESR Quantum Information Processor

A natural first experiment for a newly constructed ESR QIP spectrometer is to characterize, or *benchmark* the quality with which it operates. A suitable test of the system would allow us to compare against different technologies, to quantify any engineering improvements against relevant parameters, and give a rough measure of our system's prospects as a fault tolerant QIP architecture.

The challenge of any realization of a quantum information processor is to experimentally perform quantum operations with low error probability. Error thresholds for scalable, fault-tolerant quantum computing are generally thought to be on the order of 10^{-4}[35]. While quantum process tomography[11] may be used to determine the complete error behaviour of a quantum system, it scales poorly ($16^n - 4^n$ [8]) in the number of qubits, is limited by preparation and readout errors and does not examine behavior of gates as part of a long sequences.

Recently, a *Randomized Benchmarking* algorithm has been formalized by Knill et al. [35] to estimate the errors caused by quantum control operations. Randomized benchmarking involves applying gate sequences of varying length to a standard initial state, and measuring the increase in error probability as a function of the length of the sequence. By averaging over randomized gate sequences, randomized benchmarking extracts a single, computationally relevant value, called the average gate fidelity. The protocol is not

sensitive to preparation and measurement procedures, and the stability of errors over long sequences are verified inherently.

It should be noted that related work has been done by our collaborator, J. J.L. Morton, where the rotation angle, and phase errors of a commercial ESR spectrometer were measured using CP, CPMG and a new SPAM sequence. Rotation angle errors were found to be approximately 10%, and phase errors to be 1.5°as set by the factory, but could be improved to 0.3°using the SPAM sequence [38].

4.1 Single Qubit Algorithm

The single qubit randomized benchmarking algorithm consists of a large number of experiments, each experiment involving an identical state preparation; a pulse sequence of random, alternating π and $\pi/2$ pulses; and a final measurement. The $\pi/2$ pulses are chosen uniformly randomly to be about the $\pm\{x, y\}$ axes, and represent computational gates. The length of a sequence is considered to be the number of computational gates or $\pi/2$ pulses. The alternating π pulses are chosen from $\pm\{x, y, z, \mathbb{I}\}$, and serve as Pauli randomizations to the computational gates. The final computational gate is called a recovery gate and must be chosen to return the state to the measurement axis, ensuring that the outcome may be predicted in the absence of errors. A visualization of an individual benchmarking sequence is shown in Figure 4.1.

By averaging the results of repeated Pauli randomizations of a sequence, and by further randomizing by averaging over other sequences of random computational gates, it has been shown [47, 14] that the protocol effectively forms a depolarizing channel. Thus the fidelity decays exponentially with the number of gates, and fitting the decay yields an estimate of the errors per gate.

The single qubit algorithm proposed by Knill et al. proceeds as follows:

1. Choose a set of N_L different lengths l_j of computational sequences to be tested, i.e. $N_L = 20$, and $l_j = \{2, 3, 4, 5, 6, 8, 10, 12, 16, 20, 24, 32, 40, 48, 64, 80, 96, 128, 160, 192\}$.

2. Choose N_S sequences $\{s_i\}$ of random computational gates, each sequence having the
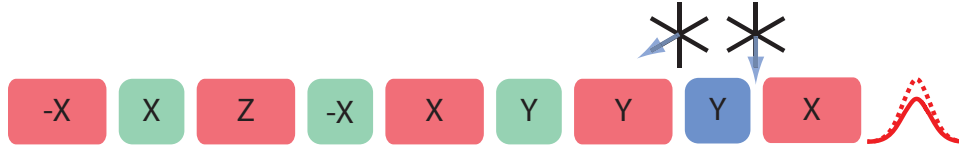
Figure 4.1: An individual randomized benchmarking sequence visualization. The longer, red squares represent Pauli (π) gates; the shorter, green squares represent computational ($\pi/2$) gates; the blue square represents a recovery gate chosen in this case to return spins from the positive x-axis to the negative z-axis; and the last icon represents a spin-echo measurement of the z-magnetization and comparison to a reference.

maximum number of gates chosen previously, i.e. $N_S = 4$, and each $\{s_i\}$ composed of 192 random gates.

3. Choose a number of Pauli randomizations that will be performed i.e. $N_P = 8$

4. For each of the N_S computational gate sequences, $\{s_i\}$, do the following:

   (a) Truncate a sequence $\{s_i\}$ at each of the l_j lengths chosen previously.

   (b) For each truncation of the current sequence s_i do the following:

      i. For each number of Pauli randomizations N_P do the following

         A. Insert randomly selected Pauli gates into the truncated sequence between each computational gate

         B. Calculate the result of applying the sub-sequence of ideal computational gates to a common initial state.

         C. Append a recovery computational gate, selected such that its action returns the state to a common measurement axis (i.e. the Z-axis) in either direction with equal probability.

         D. Append a final Pauli gate to the sequence. The sequence now begins and ends with Pauli gates, and has one between every computational gate.

         E. Calculate the expected direction of the state after the complete sequence

         F. Experimentally apply the prepared sequence to the fixed initial state

         G. Measure the resulting state and compare with a reference state

43

The typical values of $N_L = 20$, $N_S = 4$ and $N_P = 8$ amount in 640 individual experiments, with $N_S \times N_P = 32$ averaged points per length. Fitting the exponential decay gives the average depolarization probability d, which is related to the average error per gate $(1 - F_{ave}) = d/2$.

4.2 Collaboration

To ensure the randomized benchmarking measurements taken with our new spectrometer are consistent with the ESR state-of-art, randomized benchmarking should be performed on a widely-adopted, commercial ESR spectrometer. Bruker BioSpin is the only vendor offering commercial, pulsed ESR spectrometers. Fortunately, one of the few Bruker Elexsys E580 ESR spectrometers in Canada is located nearby at Brock University, St. Catharines, Ontario. Even before our own spectrometer was ready, Professor Art Van der Est from the Department of Chemistry at Brock kindly allowed us time on his E580 spectrometer.

In addition, a sample of paramagnetic material suitable for randomized benchmarking had to be found or chemically synthesized, potentially requiring considerable expertise and equipment. To this end, we approached Dr. John J. L. Morton, Co-Leader of the Quantum Spin Dynamics Group at the Department of Materials, University of Oxford; whom has done extensive research with the paramagnetic material N@C_{60}. Through a collaboration with Dr. Morton's group, we also gain access to another Bruker E580 spectrometer at the University of Oxford, and expertise in its use for QIP. Dr. Morton has mediated a collaboration with Dr. Kyriakos Porfyrakis, Head of the Laboratory for Carbon Nanomaterials at the University of Oxford, whose group has graciously synthesized a sample of N@C_{60} for use in the randomized benchmarking experiment.

4.3 N@C_{60}

Shown in Figure 4.2(a), nitrogen-incarcerated fullerene (N@C_{60}) consists of an isolated nitrogen atom inside the hollow fullerene cage. The electron spin of the defect is $S = 3/2$, and in our case the abundant isotope ^{14}N is used for implantation which has spin $I = 1$. Also depicted in Figure 4.2(a) is the production of N@C_{60} by simultaneous ion
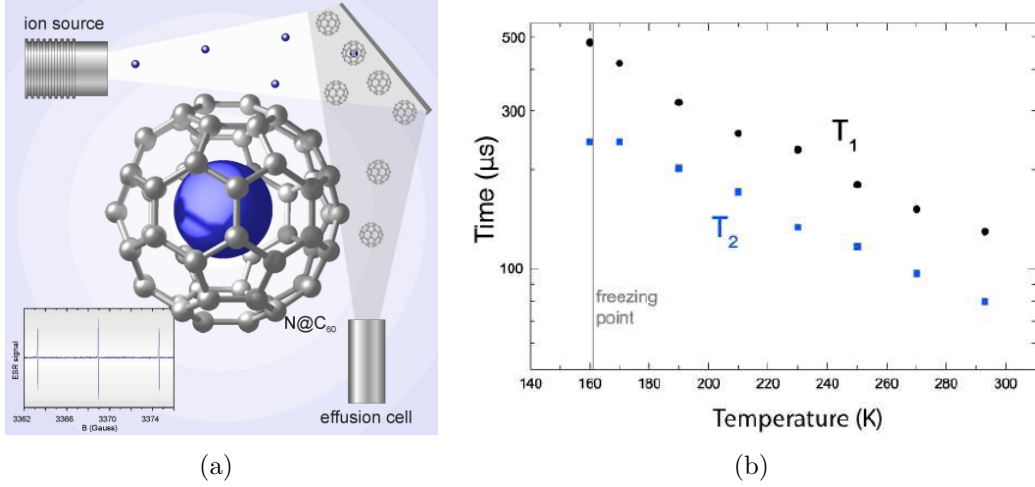
Figure 4.2: N@C_{60} production and relaxation times. Figure (a) shows the nitrogen-ion bombardment of fullerene film which is continuously grown on a target by an effusion cell. (b) shows the T_1 and T_2 relaxation time of N@C_{60} dissolved in CS_2 as a function of temperature.

bombardment from a plasma discharge ion source and fullerene evaporation onto a target under vacuum [4]. This procedure yields nitrogen capture rates of only around 10^{-4}. The mixture of N@C_{60}, empty fullerenes, and damaged fullerenes may then be dissolved in toluene and purified by high performance liquid chromatography (HPLC) which is made extremely challenging by the chemical similarity of N@C_{60} and C_{60} [31]. Once purified, the N@C_{60} is dissolved in carbon di-sulfide (CS_2) to an approximate concentration of $10^{15}/cm^3$, where it has been shown to have extremely long relaxation times of $80\mu s$ T_2, and $120\mu s$ T_1 at room temperature[39] (see 4.2(b)).

N@C_{60} in CS_2 is an ideal sample for single qubit benchmarking as the electron spin is a well isolated qubit with extremely narrow linewidth and long relaxation times. The ESR spectrum, shown as an inset in 4.2(a), has three lines separated by 15MHz due to the isotropic hyperfine interaction with spin-1 ^{14}N nucleus. All benchmarking experiments are done using the centre line of the triplet, corresponding to the nitrogen nuclear spin projection $M_I = 0$. Given the small isotropic hyperfine coupling, simultaneous flips of electron and nuclear spins are largely forbidden and the electron spin evolution may be treated individually for each nuclear spin manifold. It can be shown that the evolution of the electron spin in the $M_I = 0$ manifold is largely unaffected by the presence of the

t_{90}	t_{180}	Pulse Spacing	d	Error per gate
10ns	20ns	0	3.3×10^{-4}	1.7×10^{-4}
56ns	112ns	0	1.9×10^{-3}	9.3×10^{-4}
56ns	112ns	50ns	3.0×10^{-3}	1.5×10^{-3}

Table 4.1: Estimated depolarization factor, d, and average gate error, $d/2$, for N@C$_{60}$ dissolved in CS$_2$ for various combinations of pulse lengths and spacing between pulses. Estimates were made using equation 4.1, with 80μs for T$_2$ and 120μs for T$_1$.

t_{90}	t_{180}	Pulse Spacing	d	Error per gate
10ns	20ns	0	4.1×10^{-3}	2.0×10^{-3}
56ns	112ns	0	2.3×10^{-2}	1.1×10^{-2}
56ns	112ns	50ns	3.5×10^{-2}	1.8×10^{-2}

Table 4.2: Estimated depolarization factor and average gate error using an approximate T$_2^*$ for the spectrometer instead of T$_2$ in equation 4.1. Lower error rates than predicted by T$_2^*$ are expected since the benchmarking sequence partially refocusses static field inhomogeneities.

hyperfine coupling and can be adequately described by the usual Bloch sphere visualization of a single spin. [38]

Equation 4.1, derived in the Laforest thesis [36], can be used to estimate the depolarization factor expected only from the relaxation rates of N@C$_{60}$ in CS$_2$, assuming perfect control otherwise:

$$d = 1 - \frac{e^{-\frac{t}{T_1}} + 2e^{-\frac{t}{T_2}}}{3} \tag{4.1}$$

Using the values of, $T_1 = 120\mu$s and $T_2 = 80\mu$s, Table 4.1 shows the depolarization factors d, and average gate errors $d/2$. Table 4.2 shows the expected values if an approximate value of spectrometer T$_2^*$= 5μs is used instead of T$_2$ in the calculation. As the Pauli gates in the randomized benchmarking sequence somewhat refocus inhomogeneities in the static field contributing to T$_2^*$, we should expect an error rate somewhat lower than T$_2^*$ predicts, but higher than the T$_2$ prediction.

4.4 Simulations

A simple ESR simulator was written by C.A. Ryan which features a distribution of the natural Hamiltonian (i.e. B_0 inhomogeneity) and incorporates decoherence by propagating a Lindbladian master equation. For basic simulations, an isolated free electron was modeled with a T_2 decoherence of $80\mu s$ and a field inhomogeneity distribution of 5MHz (roughly that observed on the actual spectrometer).

The first insights from the simulator showed us that one of our pulse power calibration procedures may not be effective. Intuitively, one may expect repeated application of 90 degree pulses around the same axis to produce an oscillating pattern as the spin magnetization is rotated alternatively between the x-y and z planes—a kind of discretized Rabi experiment. The pulse power could be calibrated by making adjustments such that every other point approached zero signal integral. However, this multiple-90-pulse experiment did not take into account the effect of refocussed spin echoes caused by combinations of delays between the many pulses. Figure 4.3(a) shows the simulation of the experiment with perfectly calibrated pulses. After two 90 degree pulses (magenta spike), one may think the magnetization vector has rotated from +Z, through -Y, to -Z and thus not be detected. Integrating the signal for some time after the 2 pulses would show a large error with this logic, since a spin-echo has formed from the first two pulses. Figure 4.3(b) shows the experimental results which match qualitatively with the simulation. Thanks to the simulator, this sequence is no longer used for calibration, and has been replaced with the CP sequence.

The benchmarking sequence was then simulated under a variety of conditions. Figure 4.4 shows reference simulations for benchmarking under ideal conditions. Using the simulator, pulses can be perfectly calibrated, and in this case the durations are 10ns ($\pi/2$) and 20ns (π), with no spaces between pulses. Only the $80\mu s$ T_2 and 5MHz field distribution errors remain. Figure 4.4(a) shows the results from all 640 simulated experiments, 32 points per length. We see the distribution is very tight, since there are virtually no systematic errors. Figure 4.4(b) shows the averaging over the 8 Pauli randomizations, leaving an average for each of the 4 sequences of gates. This plot can be useful to identify adverse errors in specific sequences. 4.4(c) shows the additional average over the 4 sequences, leaving 1 point per length, which is fitted to extract the depolarization parameter. The exponential
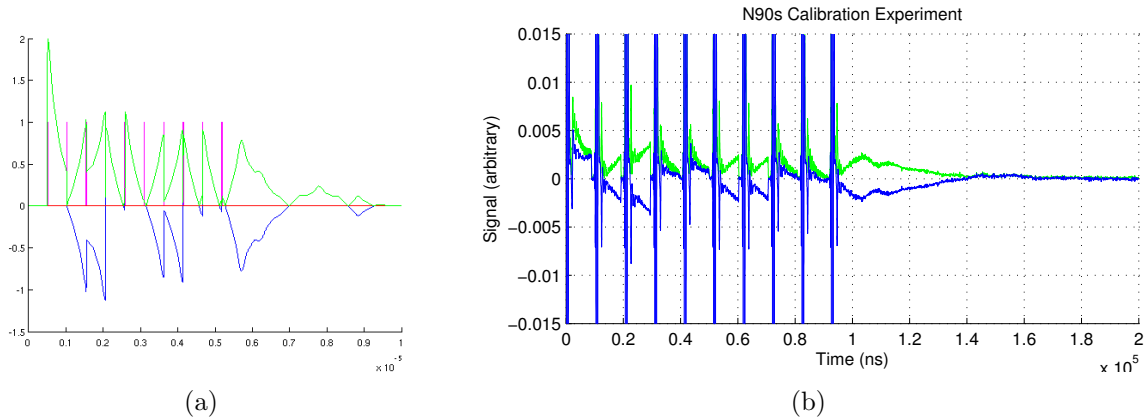
Figure 4.3: A repeated-90 pulse simulation vs. experiment. Green signals represent the absolute value of the complex signal, and blue represent the real part. (a) shows the simulator prediction, and (b) the experimental result. The simulator qualitatively predicts the resulting experimental echo. In experiment, the pulse leakage into the receiver is significant as visible as major spikes in the plot.

fit yields a parameter of 0.00025, or an average error per gate of 1.3×10^{-4}. Finally, 4.4(d) shows the spin echo measurement from an individual benchmarking sequence, which has been considerably distorted by T_2^* echoes.

With a benchmarking reference simulated, various expected errors can now be examined. (a) shows the effect of a simulated 10% rotation angle (pulse power/duration) error. To simulate a pulse power or duration miscalibration, the pulse lengths were reduced to 9ns ($\pi/2$) and 18ns (π). The results are dramatic. Systematic errors of this kind manifest in significant variance in the results. When averaged, the mean quickly tends to zero, dragging down the error per gate. This experiment yielded a dismal 3.3e-2 (3.3%) average error per gate.

Figure 4.5(b) shows the effects of rotation axis errors (microwave pulse phase). A different phase error up to $\pm 10°$ was chosen randomly for each of the four major axis phases in the spectrometer. The phases were thus $\phi_{+x} = 3°$, $\phi_{+y} = 83°$, $\phi_{-x} = 184°$ and $\phi_{-y} = 261°$. The effect is not as dramatic as the angle error experiment, however the systematic errors are apparent. The fit yielded an average error per gate of 2×10^{-2}.

A simulation of increased pulse spacing is shown in Figure 4.5(c), and an individual echo from the experiment is shown in 4.5(d), the result from a sequence of length 80.
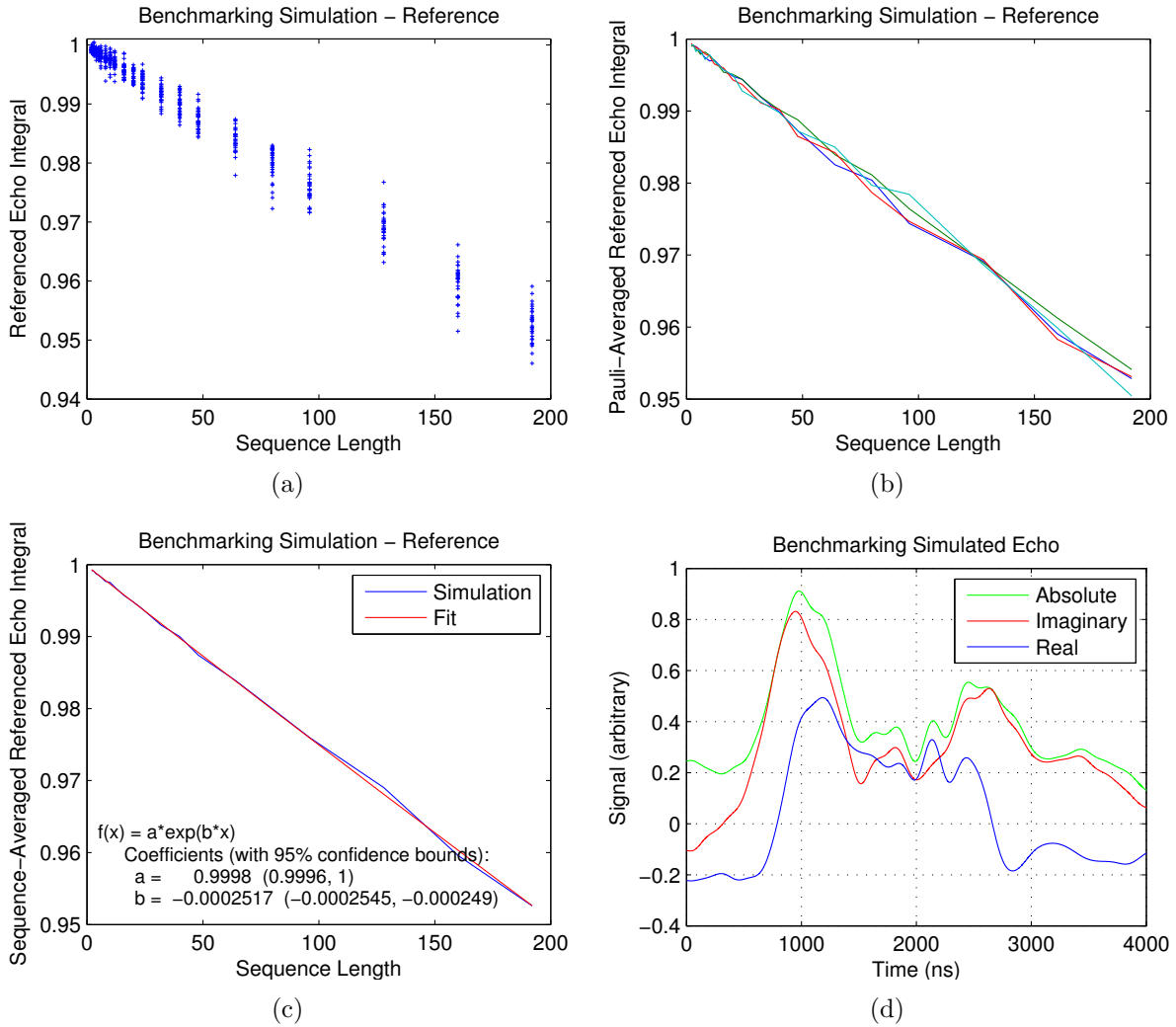
Figure 4.4: Benchmarking reference simulation, with averaging steps shown individually. The simulated parameters were 10ns and 20ns $\pi/2$ and π pulses, with no pulse spacing, and a 4μs integration window. In (a), the results of all 640 simulations are plotted, 32 points per length. In (b), each length has been averaged over the 8 Pauli randomizations. At this stage, each randomized sequence can be inspected for adverse error behaviour. In (c), each length has been further averaged over the 4 different computational sequences, leaving one point per length. The fit gives a depolarization parameter of 0.00025, for an average error per gate of 1.3×10^{-4}. (d) shows a simulated echo from an individual pulse sequence of computational length 96. In the simulation, the imaginary (red) signals are integrated.

49

Contrary to the other errors, pulse spacing demonstrates a largely coherent error, as the variance remains small but the exponential damping is large. The fit yielded an average error per gate of 5×10^{-3}.

In addition, we have simulated the effects of the phase droop from our TWT amplifier, the results supporting some experimental observations. Figure 4.6(a) shows the simulation result, and the resulting non-exponential decay. Under a phase droop error, performance of the gates depends on the length of the sequence, hence benchmarking does not work. Figure 4.6(b) shows an experimental result whose cause was not immediately obvious until after the simulation.

Finally, we simulate the depolarization of randomized benchmarking on the spin-echo measurements. Though the measured echo results such as figures 4.4(d) and 4.5(d) bear little resemblance to their reference echo, upon the averaging steps of benchmarking, the noise is depolarized and an echo shape is recovered, as shown in 4.7. This simulation did not introduce any artificial control errors.

Benchmarking simulations are invaluable in understanding results, and evaluating and pursuing the future directions, as discussed in section 4.7.

4.5 Experimental Results

Using our home-built ESR spectrometer, 5-loop-4-gap resonator and $N@C_{60}$ in CS_2 sample, preliminary benchmarking experiments have been performed, with a typical result shown in Figure 4.8. Using 56ns ($\pi/2$) and 112ns (π) Gaussian shaped pulses, we have measured average gate errors of 7×10^{-3}, which is within the expected region between the T_2^* estimate of 1.8×10^{-2} and the T_2 estimate of 1.5×10^{-3}. Since the decoherence limit has not been reached, there is room for improvement in the control, and these numbers are expected to improve with further work (see Section 4.7). Table 4.3 shows how our preliminary ESR single qubit benchmarking results compare to other realizations.

Preliminary benchmarking experiments have started on a Bruker Elexsys e580 commercial spectrometer at the University of Oxford and Brock University, however due to the novelty and demands of this type of experiment, satisfactory results have yet to be achieved.
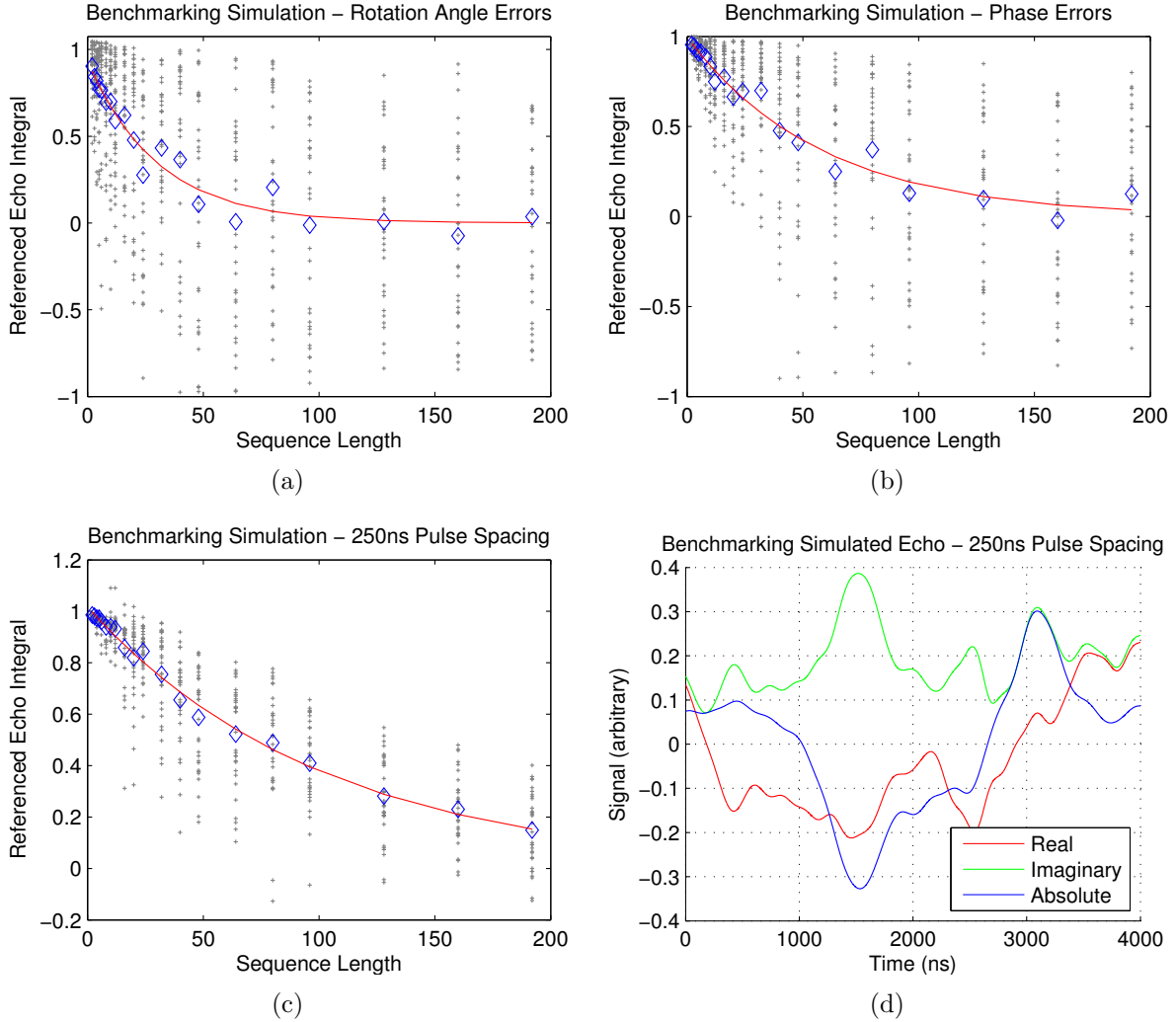
Figure 4.5: Randomized benchmarking experimental error simulations. In (a), a 10% rotation angle (pulse duration) error was simulated, which has a drastic effect on the variance of benchmarking outcomes. Fitting gives an average error per gate of 3.3×10^{-2}. In (b), a rotation axis (pulse phase) error of up to 10 degrees per phase channel is simulated. Average gate error is 2×10^{-2} In (c), the spacing between pulses is increased to 250ns. In this case we see a stronger effect from decoherence than the systematic errors of (a) and (b), i.e. the variation is less harmful than the overall reduced mean value. Average gate error is 5×10^{-3}. (d) shows a simulated echo from an individual experiment of computational length 80 with 250ns spacing.
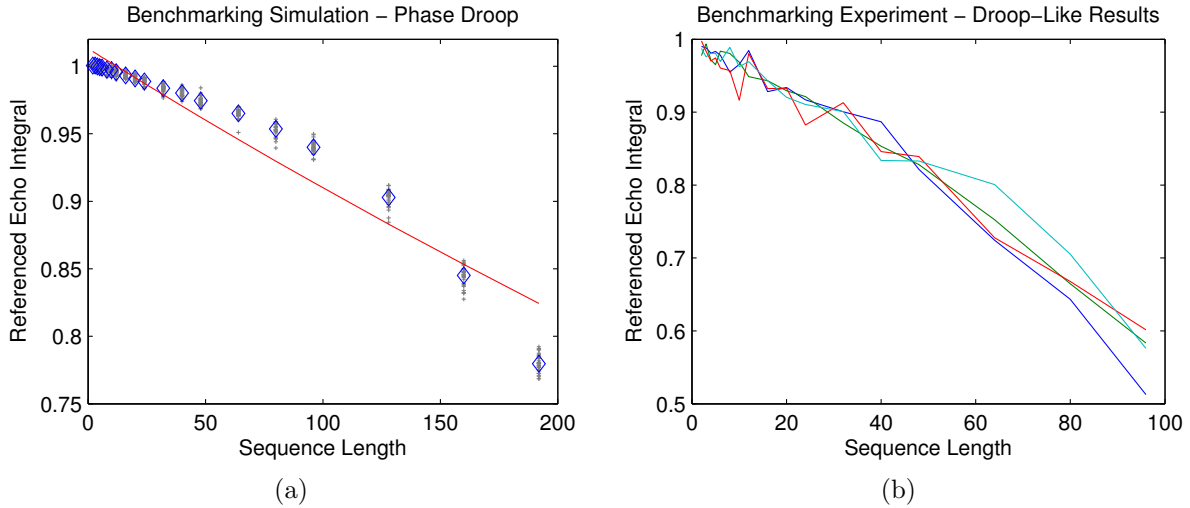
Figure 4.6: Effects of phase droop on benchmarking. Phase droop means that gate errors are not independent of the gate location in the sequence, and an exponential decay can not be fit to the results. (a) shows a simulation of the measured amplifier phase droop and no other control errors. (b) shows an experimental result that appears to demonstrate droop-like effects (downward concavity).

Group	Qubit	Average Error Per Gate	Reference
Schoelkopf	Superconducting Transmon (2009)	0.011	[10]
Schoelkopf	Superconducting Transmon (2010)	0.007	[9]
Laflamme	**ESR (N@C$_{60}$)**	**0.007**	
Knill	Trapped Ion (Paul Trap)	0.00482	[35]
Biercuk	Trapped Ion (Penning Trap)	0.0008	[7]
Porto	Neutral Atom	0.00014	[43]
Laflamme	Liquid-State NMR	0.00013	[47]

Table 4.3: Benchmarking Results of All Groups and Realizations to Date. Our preliminary result is highlighted in bold.
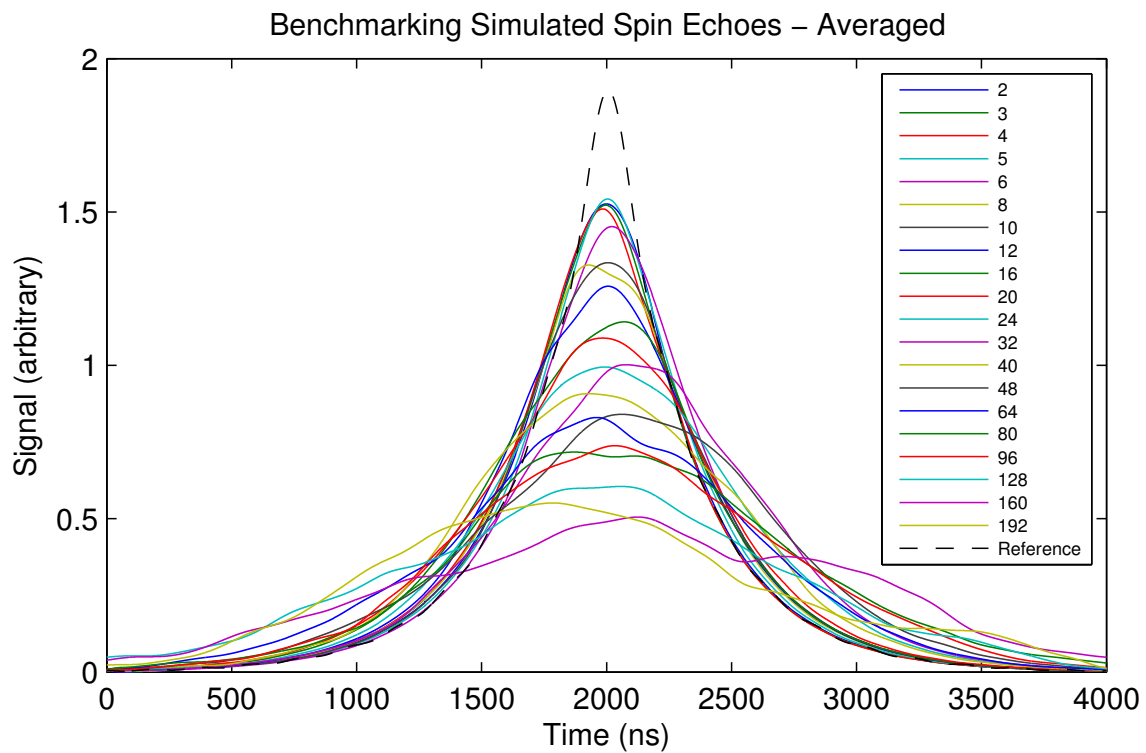
Figure 4.7: Simulated averaging of individual benchmarking spin echoes with no artificial control errors. Although individual runs may not resemble the reference spin-echo whatsoever, averaging over Paulis and sequences depolarizes the errors and produces a more recognizable result.
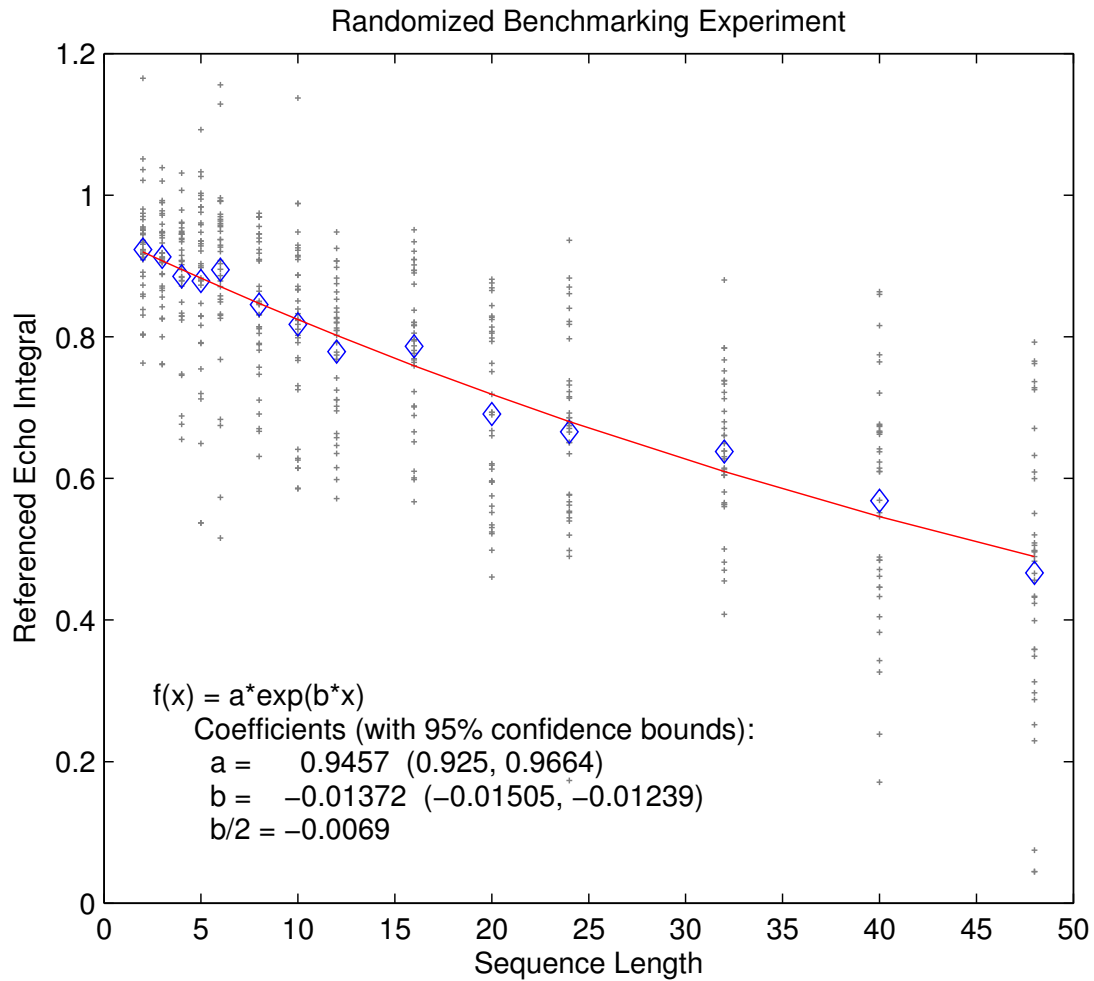
Figure 4.8: Experimental benchmarking results on the home-built ESR spectrometer using N@C$_{60}$ sample at room temperature. Computational, $(\pi/2)$ gates were 56ns Gaussian shaped pulses, and Pauli (π) gates were 112ns Gaussian shaped pulses. No spacing between pulses was used. The blue line represents the mean of all sequences and Pauli randomizations at each truncation length. In red is an exponential fit to the mean, with the fitting coefficients displayed. The average gate error measured in this experiment was 0.0069.

4.6   Sources of Error

Using randomized benchmarking, we have demonstrated average gate errors of 7×10^{-3} per gate. Several sources of error in the spectrometer and sample contribute to this value, such as:

- Static magnetic field (B_0) inhomogeneity – only partially refocussed by the benchmarking scheme, contributes to T_2^*, and the primary cause of the distorted echo shapes

- Static field instability – affects the frequency of the final result, and the efficiency of pulses on the spins. Could contribute to T_2^*

- RF field (B_1) inhomogeneity – spins that do not experience the intended control fields rapidly accumulate errors

- Phase droop, phase stability of spectrometer electronics

- Pulse mis-calibration – calibration procedures are subject to noise and other errors in the spectrometer and have finite accuracy

- Spin relaxation in the sample

4.7   Future Work

A few avenues to improve the benchmarking results are known but have yet to be implemented:

1. Tables 4.1 and 4.2 show us that considerable gains are possible simply by shortening the pulse lengths (increasing the pulse power) and reducing pulse spacing, decreasing the impact of decoherence. While mixed results from varying these parameters have previously been observed, the new insight provided by the simulations should motivate and aid with future investigations. A previous speculation was that decreased

pulse spacing combined with resonator ringdown causes pulses to blend together leading to rotations around undesired axes. These effects should be reduced or eliminated by using Gaussian shaped pulses instead of square shapes.

2. The amplifier phase droop can be corrected with pulse-fixing.

3. BB1 composite pulses [58], robust to RF field variations and successfully used for liquid-state NMR benchmarking [47] should be explored. An RF-selection sequence should also be considered, to select only spins that experience the ideal control fields. Together, these techniques should correct for much of the error due to RF inhomogeneity.

4. A new magnetic field controller will stabilize the field, making calibration experiments more accurate, and the results stable for long periods. The controller will also be computer controlled, allowing for automated field correction using ESR data, i.e. a field-frequency lock. Since reference spectra are frequently taken as a part of benchmarking, a field-frequency lock requires little overheard and is a natural extension.

5. A sample with longer relaxation times, such as phosphorus-doped 28-silicon at low temperature could be used instead of N@C$_{60}$.

Chapter 5

Conclusions

In this thesis, we have presented a home built ESR spectrometer designed specifically for quantum information processing. The system will have excellent magnetic field stability of 0.1ppm, an extremely stable and spectrally pure microwave source, arbitary phase and amplitude modulation of pulses to 1ns time resolution, up to 1kW of microwave pulse power, digital demodulation, fast signal averaging and flexible software. All of these characteristics are extremely desirable for ESR QIP and make this spectrometer cutting-edge in that respect.

Loop-gap resonators and variable temperature probes have been designed and built. The rising-sun resonator has shown an adjustable quality factor by overcoupling from Q=1000 to Q<300 demonstrating its versatility for future CW or ENDOR versions of the probe.

The randomized benchmarking algorithm by Knill et al. has been simulated under various conditions and preliminary experiments have been carried out. An average error probability on the order of 10^{-3} errors per gate has been demonstrated on a custom-built ESR spectrometer for QIP. The result is not limited by the relaxation in the sample, thus there is room for improvement in the control. Other contributions to gate errors arise from static magnetic field (B_0) inhomogeneity and instability, RF field (B_1) inhomogeneity, phase droop and stability of spectrometer electronics, pulse mis-calibration. The value is expected to improve with shorter pulses, pulse fixing, composite pulses, and RF-selection sequences. Collaborators are in the process of running randomized benchmarking on com-

mercial ESR spectrometers to validate our results.

Our randomized benchmarking results are encouraging, demonstrating that the control of a single qubit in our ESR spectrometer is approaching thresholds for fault tolerant quantum computing. Using the spectrometer to identify and benchmark improvements in technology and technique shows the usefulness of the system as a testbed for electron spin control towards a successful implementation of a quantum information processor.

References

[1] Ieee standard letter designations for radar-frequency bands. *IEEE Std 521-2002*, 2003.

[2] A. Aassime, G. Johansson, G. Wendin, R. J. Schoelkopf, and P. Delsing. Radio-frequency single-electron transistor as readout device for qubits: Charge sensitivity and backaction. *Phys. Rev. Lett.*, 86(15):3376–3379, Apr 2001.

[3] Mohamed Osama Abutaleb. Rf instrumentation and system design for coherent control of anisotropic hyperfine-coupled electron/nuclear spin qubits. Master's thesis, Massachusetts Institute of Technology, 2010.

[4] T. Almeida Murphy, Th. Pawlik, A. Weidinger, M. Höhne, R. Alcala, and J.-M. Spaeth. Observation of atomlike nitrogen in nitrogen-implanted solid c_{60}. *Phys. Rev. Lett.*, 77(6):1075–1078, Aug 1996.

[5] Gopalakrishnan Balasubramanian, Philipp Neumann, Daniel Twitchen, Matthew Markham, Roman Kolesov, Norikazu Mizuochi, Junichi Isoya, Jocelyn Achard, Johannes Beck, Julia Tissler, Vincent Jacques, Philip R. Hemmer, Fedor Jelezko, and Jorg Wrachtrup. Ultralong spin coherence time in isotopically engineered diamond. *Nat Mater*, 8(5):383–387, 05 2009.

[6] SC Benjamin, A Ardavan, G Andrew, D Briggs, DA Britz, D Gunlycke, J Jefferson, MAG Jones, DF Leigh, BW Lovett, AN Khlobystov, SA Lyon, JJL Morton, K Porfyrakis, MR Sambrook, and AM Tyryshkin. Towards a fullerene-based quantum computer. *Journal of Physics-Condensed Matter*, 18(21):S867–S883, May 2006.

[7] Michael J. Biercuk, Hermann Uys, Aaron P. VanDevender, Nobuyasu Shiga, Wayne M. Itano, and John J. Bollinger. High-fidelity quantum control using ion crystals in a penning trap. 06 2009.

[8] Andrew M. Childs, Isaac L. Chuang, and Debbie W. Leung. Realization of quantum process tomography in nmr. *Phys. Rev. A*, 64(1):012314, Jun 2001.

[9] J. M. Chow, L. DiCarlo, J. M. Gambetta, F. Motzoi, L. Frunzio, S. M. Girvin, and R. J. Schoelkopf. Implementing optimal control pulse shaping for improved single-qubit gates. 05 2010.

[10] J. M. Chow, J. M. Gambetta, L. Tornberg, Jens Koch, Lev S. Bishop, A. A. Houck, B. R. Johnson, L. Frunzio, S. M. Girvin, and R. J. Schoelkopf. Randomized benchmarking and process tomography for gate errors in a solid-state qubit. *Phys. Rev. Lett.*, 102(9):090502, Mar 2009.

[11] I. L. Chuang and M. A. Nielsen. Prescription for experimental determination of the dynamics of a quantum black box. *Journal of Modern Optics*, 44(11):2455–2467, November 1997.

[12] David P. Divincenzo. The physical implementation of quantum computation. *Fortschritte der Physik*, 48(9-11):771–783, 2000.

[13] M. V. Gurudev Dutt, L. Childress, L. Jiang, E. Togan, J. Maze, F. Jelezko, A. S. Zibrov, P. R. Hemmer, and M. D. Lukin. Quantum Register Based on Individual Electronic and Nuclear Spin Qubits in Diamond. *Science*, 316(5829):1312–1316, 2007.

[14] Joseph Emerson, Robert Alicki, and Karol Życzkowski. Scalable noise estimation with random unitary operators. *Journal of Optics B: Quantum and Semiclassical Optics*, 7(10):S347, 2005.

[15] W. Froncisz, T. Oles, and James S. Hyde. Q-band loop-gap resonator. *Review of Scientific Instruments*, 57(6):1095–1099, 1986.

[16] Torsten Gaebel, Michael Domhan, Iulian Popa, Christoffer Wittmann, Philipp Neumann, Fedor Jelezko, James R. Rabeau, Nikolas Stavrias, Andrew D. Greentree, Steven Prawer, Jan Meijer, Jason Twamley, Philip R. Hemmer, and Jorg Wrachtrup.

Room-temperature coherent coupling of single spins in diamond. *Nat Phys*, 2(6):408–413, 06 2006.

[17] R. Hanson, O. Gywat, and D. D. Awschalom. Room-temperature manipulation and decoherence of a single spin in diamond. *Phys. Rev. B*, 74(16):161203, Oct 2006.

[18] R. Hanson, F. M. Mendoza, R. J. Epstein, and D. D. Awschalom. Polarization and readout of coupled single spins in diamond. *Phys. Rev. Lett.*, 97(8):087601, Aug 2006.

[19] Ronald Hanson. Quantum information: Mother nature outgrown. *Nat Mater*, 8(5):368–369, 05 2009.

[20] W Harneit, C Meyer, A Weidinger, D Suter, and J Twamley. Architectures for a spin quantum computer based on endohedral fullerenes. *Physica Status Solidi B-Basic Research*, 233(3):453–461, October 2002.

[21] Wolfgang Harneit. Fullerene-based electron-spin quantum computer. *Phys. Rev. A*, 65(3):032322, Feb 2002.

[22] Jonathan Stuart Hodges. *Engineering coherent control of quantum information in spin systems*. PhD thesis, Massachusetts Institute of Technology. Dept. of Nuclear Science and Engineering., 2007.

[23] L. C. L. Hollenberg, A. S. Dzurak, C. Wellard, A. R. Hamilton, D. J. Reilly, G. J. Milburn, and R. G. Clark. Charge-based quantum computing using single donors in semiconductors. *Phys. Rev. B*, 69(11):113301, Mar 2004.

[24] James S. Hyde. Trends in epr technology. In Sandra R. Eaton, Gareth R. Eaton, and Lawrence J. Berliner, editors, *Biomedical EPR, Part B: Methodology, Instrumentation, and Dynamics*, volume 24/B of *Biological Magnetic Resonance*, pages 409–428. Springer US, 2005.

[25] R. A. Isaacson, C. Lulich, S. B. Oseroff, and R. Calvo. Coaxial coupler for a 9 ghz epr/endor cryostat. *Review of Scientific Instruments*, 51(10):1409–1411, 1980.

[26] F. Jelezko, T. Gaebel, I. Popa, M. Domhan, A. Gruber, and J. Wrachtrup. Observation of coherent oscillation of a single nuclear spin and realization of a two-qubit conditional quantum gate. *Phys. Rev. Lett.*, 93(13):130501, Sep 2004.

[27] F. Jelezko, T. Gaebel, I. Popa, A. Gruber, and J. Wrachtrup. Observation of coherent oscillations in a single electron spin. *Phys. Rev. Lett.*, 92(7):076401, Feb 2004.

[28] F. Jelezko, I. Popa, A. Gruber, C. Tietz, J. Wrachtrup, A. Nizovtsev, and S. Kilin. Single spin states in a defect center resolved by optical spectroscopy. *Applied Physics Letters*, 81(12):2160–2162, 2002.

[29] L. Jiang, J. S. Hodges, J. R. Maze, P. Maurer, J. M. Taylor, D. G. Cory, P. R. Hemmer, R. L. Walsworth, A. Yacoby, A. S. Zibrov, and M. D. Lukin. Repetitive Readout of a Single Electronic Spin via Quantum Logic with Nuclear Spin Ancillae. *Science*, 326(5950):267–272, 2009.

[30] M. N. Jirmanus. Introduction to laboratory cryogenics. Technical report, Janis Research Company, Inc., Wilmington, MA.

[31] Mito Kanai, Kyriakos Porfyrakis, G. Andrew. D. Briggs, and T. John S. Dennis. Purification by hplc and the uv/vis absorption spectra of the nitrogen-containing incar-fullerenes inc60, and inc70. *Chemical Communications*, (2):210–211, 2004.

[32] BE Kane. A silicon-based nuclear spin quantum computer. *Nature*, 393(6681):133–137, May 1998.

[33] TA Kennedy, FT Charnock, JS Colton, JE Butler, RC Linares, and PJ Doering. Single-qubit operations with the nitrogen-vacancy center in diamond. *Physica Status Solidi B-Basic Research*, 233(3):416–426, October 2002.

[34] Navin Khaneja, Timo Reiss, Cindie Kehlet, Thomas Schulte-Herbrggen, and Steffen J. Glaser. Optimal control of coupled spin dynamics: design of nmr pulse sequences by gradient ascent algorithms. *Journal of Magnetic Resonance*, 172(2):296 – 305, 2005.

[35] E. Knill, D. Leibfried, R. Reichle, J. Britton, R. B. Blakestad, J. D. Jost, C. Langer, R. Ozeri, S. Seidelin, and D. J. Wineland. Randomized benchmarking of quantum gates. *Phys. Rev. A*, 77(1):012307, Jan 2008.

[36] Martin Laforest. Error characterization and quantum control benchmarking in liquid state nmr using quantum information processing techniques. Master's thesis, University of Waterloo, 2008.

[37] JJL Morton, AM Tyryshkin, A Ardavan, K Porfyrakis, SA Lyon, and GAD Briggs. Measuring errors in single-qubit rotations by pulsed electron paramagnetic resonance. *Physical Review a*, 71(1), January 2005.

[38] John J. L. Morton, Alexei M. Tyryshkin, Arzhang Ardavan, Kyriakos Porfyrakis, S. A. Lyon, and G. Andrew D. Briggs. Measuring errors in single-qubit rotations by pulsed electron paramagnetic resonance. *Phys. Rev. A*, 71(1):012332, Jan 2005.

[39] John J. L. Morton, Alexei M. Tyryshkin, Arzhang Ardavan, Kyriakos Porfyrakis, S. A. Lyon, and G. Andrew D. Briggs. Electron spin relaxation of n@c[sub 60] in cs[sub 2]. *The Journal of Chemical Physics*, 124(1):014508, 2006.

[40] John J. L. Morton, Alexei M. Tyryshkin, Richard M. Brown, Shyam Shankar, Brendon W. Lovett, Arzhang Ardavan, Thomas Schenkel, Eugene E. Haller, Joel W. Ager, and S. A. Lyon. Solid-state quantum memory using the p-31 nuclear spin. *Nature*, 455(7216):1085–1088, October 2008.

[41] S. Nellutla, G. W. Morley, J. van Tol, M. Pati, and N. S. Dalal. Electron spin relaxation and ^{39}k pulsed endor studies on cr^{5+} -doped k_3nbo_8 at 9.7 and 240 ghz. *Phys. Rev. B*, 78(5):054426, Aug 2008.

[42] P. Neumann, N. Mizuochi, F. Rempp, P. Hemmer, H. Watanabe, S. Yamasaki, V. Jacques, T. Gaebel, F. Jelezko, and J. Wrachtrup. Multipartite Entanglement Among Single Spins in Diamond. *Science*, 320(5881):1326–1329, 2008.

[43] S. Olmschenk, R. Chicireanu, K. D. Nelson, and J. V. Porto. Randomized benchmarking of atomic qubits in an optical lattice. 08 2010.

[44] I. Popa, T. Gaebel, M. Domhan, C. Wittmann, F. Jelezko, and J. Wrachtrup. Energy levels and decoherence properties of single electron and nuclear spins in a defect center in diamond. *Phys. Rev. B*, 70(20):201203, Nov 2004.

[45] G. A. Rinard, R. W. Quine, S. S. Eaton, G. R. Eaton, and W. Froncisz. Relative benefits of overcoupled resonators vs inherently low-q resonators for pulsed magnetic resonance. *Journal of Magnetic Resonance, Series A*, 108(1):71 – 81, 1994.

[46] George A. Rinard and Gareth R. Eaton. Loop-gap resonators. In Sandra R. Eaton, Gareth R. Eaton, and Lawrence J. Berliner, editors, *Biomedical EPR, Part B: Methodology, Instrumentation, and Dynamics*, volume 24/B of *Biological Magnetic Resonance*, pages 19–52. Springer US, 2005.

[47] C A Ryan, M Laforest, and R Laflamme. Randomized benchmarking of single- and multi-qubit control in liquid-state nmr quantum information processing. *New Journal of Physics*, 11(1):013034, 2009.

[48] R. S. Said and J. Twamley. Robust control of entanglement in a nitrogen-vacancy center coupled to a ^{13}c nuclear spin in diamond. *Phys. Rev. A*, 80(3):032303, Sep 2009.

[49] R. J. Schoelkopf, P. Wahlgren, A. A. Kozhevnikov, P. Delsing, and D. E. Prober. The Radio-Frequency Single-Electron Transistor (RF-SET): A Fast and Ultrasensitive Electrometer. *Science*, 280(5367):1238–1242, 1998.

[50] Fazhan Shi, Xing Rong, Nanyang Xu, Ya Wang, Jie Wu, Bo Chong, Xinhua Peng, Juliane Kniepert, Rolf-Simon Schoenfeld, Wolfgang Harneit, Mang Feng, and Jiangfeng Du. Room-temperature implementation of the deutsch-jozsa algorithm with a single electronic spin in diamond. *arXiv:1002.2465v1*, 02 2010.

[51] Dr. Anuj Srivastava. Cost and performance benefits of cascading single junction circulators for duplex applications. *Microwave Product Digest*, June 2007.

[52] Bradley E. Sturgeon and R. David Britt. Sensitive pulsed epr spectrometer with an 8–18 ghz frequency range. *Review of Scientific Instruments*, 63(4):2187–2192, 1992.

[53] Dieter Suter and Kyungwon Lim. Scalable architecture for spin-based quantum computers with a single type of gate. *Phys. Rev. A*, 65(5):052309, Apr 2002.

[54] J. Twamley. Quantum-cellular-automata quantum computing with endohedral fullerenes. *Phys. Rev. A*, 67(5):052318, May 2003.

[55] A. M. Tyryshkin, S. A. Lyon, A. V. Astashkin, and A. M. Raitsimring. Electron spin relaxation times of phosphorus donors in silicon. *Phys. Rev. B*, 68(19):193207, Nov 2003.

[56] L. M. K. Vandersypen and I. L. Chuang. Nmr techniques for quantum control and computation. *Rev. Mod. Phys.*, 76(4):1037–1069, Jan 2005.

[57] John A Weil and James R Bolton. *Electron Paramagnetic Resonance: Elementary Theory and Practical Applications; 2nd ed.* Wiley, Hoboken, NJ, 2007.

[58] S. Wimperis. Broadband, narrowband, and passband composite pulses for use in advanced nmr experiments. *Journal of Magnetic Resonance, Series A*, 109(2):221 – 231, 1994.

[59] J. Wrachtrup, S. Kilin, and A. Nizovtsev. Quantum computation using the 13c nuclear spins near the single nv defect center in diamond. *Optics and Spectroscopy*, 91(3):429–437, 09 2001.

[60] Jamie Chiaming Yang. *Coherent control of hyperfine-coupled electron and nuclear spins for quantum information processing.* PhD thesis, Massachusetts Institute of Technology. Dept. of Nuclear Science and Engineering., 2008.

[61] Yingjie Zhang. Universal control in 1e-2n spin system utilizing anisotropic hyperfine interactions. Master's thesis, University of Waterloo, 2010.